TECHNISCHE UNIVERSITÄT WIEN
Vienna | Austria

Master Thesis

CFD Simulation and Validation of a Formula Student Car

carried out for the purpose of obtaining the degree of Master of Science (MSc or Dipl.-Ing. or DI), submitted at TU Wien, Faculty of Mechanical and Industrial Engineering, by

Michael Kirchberger

[redacted]

under the supervision of

MSc PhD Francesco Zonta,

Institute of Fluid Mechanics and Heat Transfer, E322

Vienna, January 2023

I confirm, that the printing of this thesis requires the approval of the examination board.

Affidavit

I declare in lieu of oath, that I wrote this thesis and carried out the associated research myself, using only the literature cited in this volume. If text passages from sources are used literally, they are marked as such.

I confirm that this work is original and has not been submitted for examination elsewhere, nor is it currently under consideration for a thesis elsewhere.

I acknowledge that the submitted work will be checked electronically-technically using suitable and state-of-the-art means (plagiarism detection software). On the one hand, this ensures that the submitted work was prepared according to the high-quality standards within the applicable rules to ensure good scientific practice "Code of Conduct" at the TU Wien. On the other hand, a comparison with other student theses avoids violations of my personal copyright.

[redacted]

Place and Date

Signature

Acknowledgments

I want to thank my supervisor MSc PhD Francesco Zonta for enabling me to write my diploma thesis about a topic I am interested in and passionate about.

Furthermore, I would like to express my gratitude to my parents Hermine Kirchberger and Michael Huber-Kirchberger for having a look at the grammar and spelling of this diploma thesis. Without their support my academic education would not have come this far. I would also like to thank my sister Elisabeth for her much appreciated advice.

In addition I also want to thank the eCTO of TU Wien Racing's 2022/23 season Markus Franta because without his help the experimental pressure measurements would not have been possible. Last but not least I want to thank Hannes Menegus, Christoph Adolf and the whole TU Wien Racing team for helping me with the validation of the EDGE 14.

Abstract

The generation of downforce is achieved with aerodynamic devices and nowadays it is one of the most important performance targets, which makes the difference between winning and losing. By means of TU Wien Racing's 2022/23 Formula Student contender, the EDGE 14, the CFD simulation of aerodynamic components will be analysed in terms of accuracy, quality and magnitude of results. TU Wien Racing conducts all CFD simulations in Siemens StarCCM+. This is where a straightline halfcar simulation is implemented using the EDGE 14 CAD geometry. After generating a domain to calculate the flow and assigning the surfaces to boundary conditions, a turbulence model is chosen. The k-ω model is state of the art in external aerodynamic calculations and therefore used in this application. For the discretization of the fluid, the finite volume method is chosen in combination with the so-called Trimmed Cell Mesher. After explaining where and why to use the high wall y+ approach or low wall y+ approach, a mesh refinement study is conducted. Therefore the CLA and CDA values for an infinitesimal small grid resolution using Richardson Extrapolation are calculated. The validation of these values has been done by continually refining the mesh until CLA and CDA did not change any more and mesh independence was achieved. Validation of the CFD simulation results were carried out with local pressure measurements. Therefore the absolute pressure at 61 measurement points behind the front tyre has been obtained using an aero rake. These values were used to calculate the total pressure coefficient and compare it to the simulation results. The results were satisfying and only small differences were detected. Additionally, validation using pressure taps has been carried out. 8 probes measured the surface pressure on the low pressure side of the undertray mainfoil and these results were again compared to CFD simulation results. Finally, it has been proven that the magnitude of output by the CFD simulation is higher than in real life.

Zusammenfassung

Die Erzeugung von Abtrieb durch die Verwendung von aerodynamischer Komponenten ist heutzutage eines der größten Leistungsziele und macht den Unterschied zwischen Sieg und Niederlage aus. Mithilfe des 2022/23 Formula Student Fahrzeugs von TU Wien Racing, dem EDGE 14, wird die verwendete CFD Simulation auf Genauigkeit, Qualität und Richtigkeit der berechneten Werte analysiert. TU Wien Racing führt alle CFD Simulationen mit dem Programm Siemens StarCCM+ durch. In dieser Softwareumgebung wird eine CFD Simulation aufgebaut, welche die Strömung bei Geradeausfahrt des halben Fahrzeuges berechnet. Nachdem ein Rechengebiet erzeugt wurde, in welchem die Strömung berechnet werden soll und anschließend die Randbedingungen festgelegt wurden, wird ein Turbulenzmodell gewählt. Das k-ω Modell ist heutzutage Stand der Technik in der externen Fahrzeugaerodynamik und wird daher verwendet. Zur Diskretisierung des Fluids wird die Finite Volumen Methode in Kombination mit dem Trimmed Cell Mesher verwendet. Nachdem die Vor- und Nachteile des hohen wall y+ Ansatzes und niedrigen wall y+ Ansatzes beleuchtet wurden, wird eine Netzverfeinerungsstudie durchgeführt. Hierfür werden der CLA und der CDA Wert für ein unendlich kleines Rechengitter mithilfe der Richardson Extrapolation berechnet. Die Validierung dieses Ergebnisses wird durch schrittweises Verfeinern des Rechengitters durchgeführt bis die Werte sich nicht mehr verändern und dadurch Netzunabhängigkeit erreicht wurde. Die Validierung der Ergebnisse der CFD Simulation wird mit lokalen Druckmessungen durchgeführt. Hierfür wird der Absolutdruck an 61 Messpunkten hinter dem vorderen Reifen mittels eines Aero Rakes gemessen. Die erhaltenen Absolutdruckwerte werden umgerechnet in den total Druckkoeffizienten, welche mit den Ergebnissen der CFD Simulation verglichen werden. Die Resultate waren sehr zufriedenstellend und nur kleine Unterschiede zwischen Realität und Simulation wurden entdeckt. Zusätzlich wurde noch mit sogenannten pressure taps validiert. Hierzu wurde an 8 Messpunkten am Unterboden der Oberflächendruck aufgenommen und mit den CFD Resultaten verglichen. Hier zeigte sich, dass der Abtriebswert der Simulation höher ist als jener in der Realität.

Contents

1

Introduction

The aim of this master thesis is to analyse the flow and the generated downforce around the Formula Student vehicle of TU Wien Racing. This will be achieved by the usage of the CFD Software Star CCM+. Furthermore, the simulated results will be validated using common motorsport and scientific validation techniques.

1.1 Formula Student Rules

TU Wien Racing competes in the so-called Formula Student, which is a design competition where university students design and manufacture formula style race cars [14]. Racing takes place all around Europe (Austria, Germany, Croatia, Netherlands, Czech Republic) and also in other continents at different events. Similar to Formula One there are rules which each team has to fulfil in order to be able to compete at the events. The rules compliancy of the car is the first thing that is being checked at the events and it is absolutely necessary to statisfy every rule. This process is called scrutineering and only after having successfully finished these technical inspections the cars are allowed to race at the dynamic events. There are several disciplines which are partly manually driven or driverless. The first discipline is acceleration, where the car has to travel 75 m starting from 0 m/s in the shortest time period possible. Another discipline is the so called Skidpad where teams have to drive through 2 circles and must not hit any cones, which are the borders of the circles. Autocross is pretty much like Qualifying in Formula One, here you drive around a circuit for one timed lap and attempt to achieve the fastest time possible. The last and most important dynamic event is the Endurance. An about 22 km long distance has to be completed on a similar track to Autocross and most points are awarded to the team that finishes fastest. After the Endurance event

	CV & EV	DC
Static Events:		
Business Plan Presentation	75 points	-
Cost and Manufacturing	100 points	-
Engineering Design:	150 points	150 points
Dynamic Events:		
Skidpad	50 points	-
Driverless (DV) Skidpad	75 points	75 points
Acceleration	50 points	-
DV Acceleration	75 points	75 points
Autocross	100 points	-
DV Autocross	-	100 points
Endurance	250 points	-
Efficiency	75 points	-
Trackdrive	-	200 points
Overall	1000 points	600 points

Table 1.1 – Distribution of points at the Formula Student Germany event, source: [14]

the consumed fuel or electrical energy will be measured and these values result in the last dynamic discipline: the Efficiency rating.

In addition to the dynamic disciplines there are also static disciplines: Engineering Design, Cost and Manufacturing Report and the Business Plan. The goal is to finish as high as possible compared to other universities and as a result get as many points as achievable. There are 1000 points available split in different disciplines, as you can see in Table 1.1. TU Wien Racing competes in the Electric Vehicle category (EV) and can therefore achieve a maximum of 1000 points.

1.2 Aerodynamics in Formula Student

The ultimate goal in Motorsport is to reduce Laptime. In order to figure out the performance sensitivities, the vehicle dynamics department of TU Wien Racing conducted Laptime simulations.

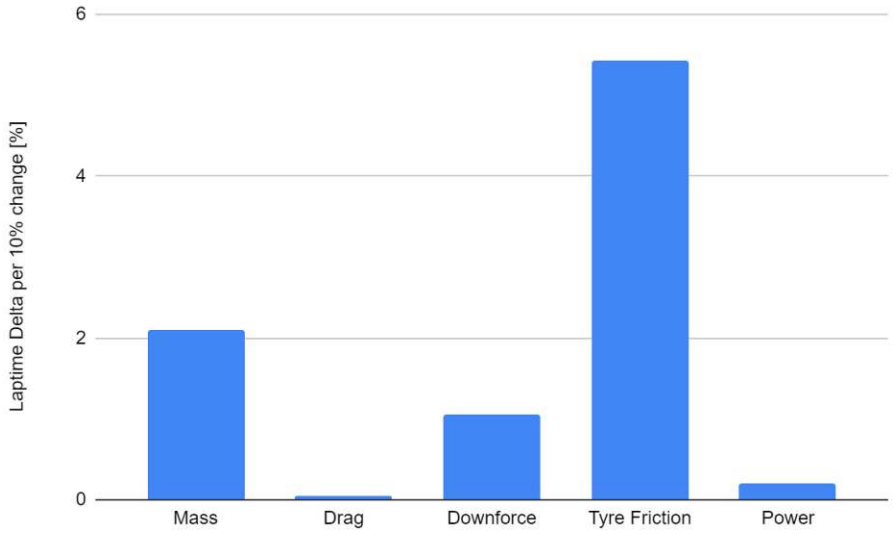

Figure 1.1 – Performance Sensitivity Study

As you can see in Figure 1.1, if you increase the downforce of the car by 10% the laptime will decrease by approximately 1%. On the other hand, it also has to be taken into account that the sensitivity of a mass increase is approximately double the sensitivity of a Downforce increase. As a result, the designer of aerodynamic elements always has to compromise between increasing the Downforce of the vehicle by adding Aerodynamic elements and adding mass and drag to the car.

The Aerodynamic package of most Formula Student cars consists of a frontwing, an undertray and a rearwing. In Figure 1.2 you can see the Aerodynamic devices of TU Wien Racing's 2023 car, the EDGE 14.

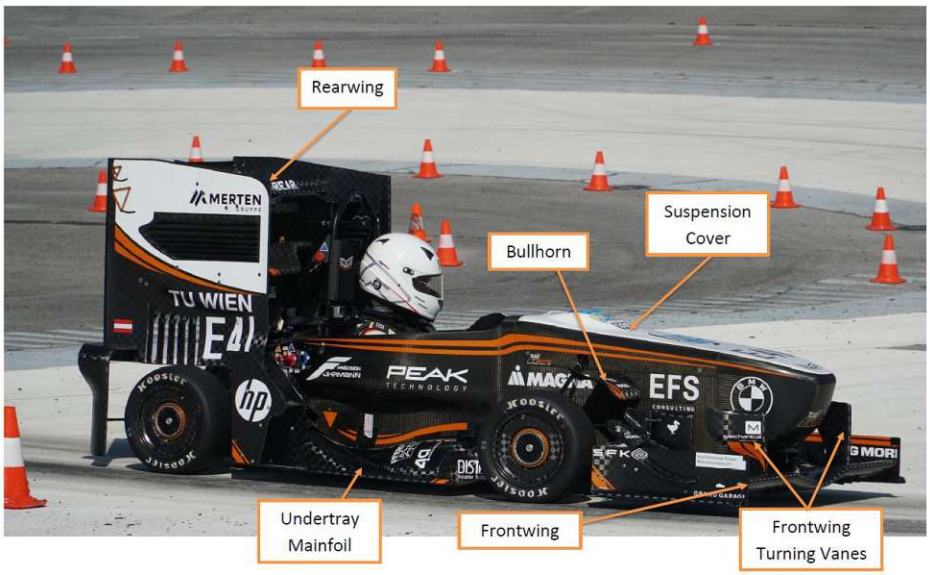

Figure 1.2 – Aerodynamic devices on the EDGE 14

In order to pass scruitineering and be allowed to compete at the events, the aerodynamic devices have to be inside a specified construction space. This rule is T8 in [14] and you can see the construction space sketched below in Fig 1.3.

	CV & EV	DC
Static Events:		
Business Plan Presentation	75 points	-
Cost and Manufacturing	100 points	-
Engineering Design	150 points	150 points
Dynamic Events:		
Skidpad	50 points	-
Driverless (DV) Skidpad	75 points	75 points
Acceleration	50 points	-
DV Acceleration	75 points	75 points
Autocross	100 points	-
DV Autocross	-	100 points
Endurance	250 points	-
Efficiency	75 points	-
Trackdrive	-	200 points
Overall	1000 points	600 points

Figure 1.3 – Aerodynamic construction space, source: [14]

In order to use the construction space as effective as possible, different concepts and approaches are designed and simulated using CFD. The next chapter will cover the buildup of the simulation in detail. After postprocessing of the conducted CFD simulation, changes are made to the design and then another simulation is started. This

iterative process is done until the goals are achieved or the design phase ends. However, this master thesis deals with the setup and validation of the simulation and not with the design of Aerodynamic components.

2

CFD Simulation

2.1 Overview

As mentioned before, the design of the Aero package is an iterative process consisting of firstly designing elements in CAD. CFD is then used as a Design Tool in order to predict the performance and to give insights into the flow characteristics [25]. For the development of the EDGE 14 approximately 250 CFD simulations in a time span of 3 months have been carried out. As a result the simulation runs must not take a long time period, but on the other hand they have to be accurate enough to argue design decisions.

Siemens is offering all Formula Student teams free usage of their CFD Software StarCCM+, which has a great user interface and is therefore easy to master. TU Wien Racing has been using it for several years and as a consequence, there already exists a baseline simulation, which has not been validated. In this chapter the different settings of the simulation will be explained.

2.2 Geometrical Setup

Computational Fluid Dynamics (CFD) is a Scientific and Engineering Analysis Tool, which solves physical laws (conservation of mass, momentum and energy) in order to get a better understanding of the flow around a defined geometry [21]. In external Aerodynamics the process starts with generating a geometry to study, and importing it to the CFD tool or directly creating it inside the CFD software. The EDGE 14 has already been designed and geometrically eased using CAD in order to directly import it into StarCCM+. The resulting volume of the vehicle can be seen in Figure 2.1.

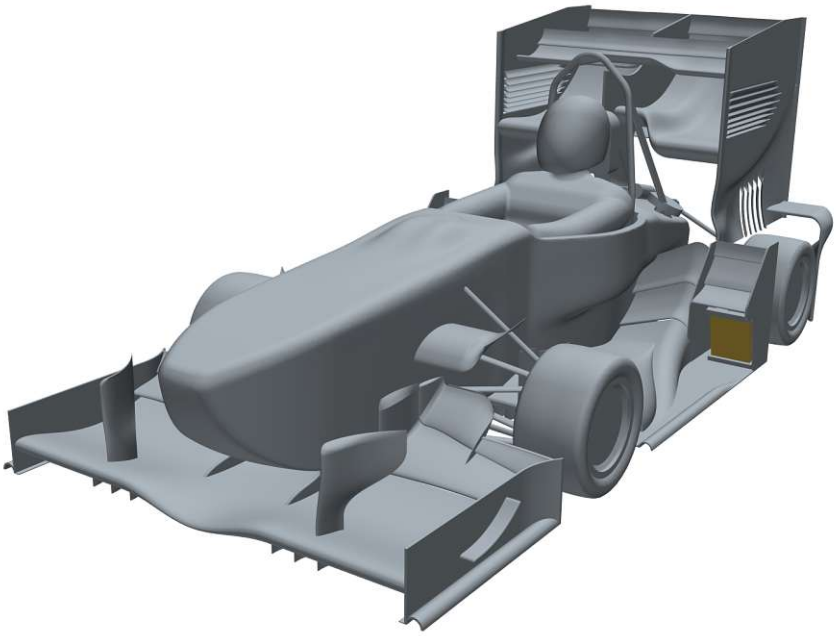

Figure 2.1 – EDGE 14 volume

The next thing is to generate a volume which represents the domain where the flow shall be simulated. As we do not want to know what the flow looks like inside the vehicle rather than around the car, a computational domain has to be created. This domain can be compared to a windtunnel and should be big enough to capture all flow phenomena around the car.On the one hand, it should be big enough not to have an impact on the solution with walls too close to the vehicle. On the other hand, it should not be too big, as the Calculation duration and Mesh generation will last longer.Based on common literature and recommendations by Siemens, the domain starts 9.5 m in front of the vehicle and reaches back for 20 m after the vehicle to capture the whole wake. Another important aspect of domain length is that it has to be long enough for the flow to be uniform at the outlet. Otherwise numerical mistakes are possible. The domain is 7 m high and 4 m wide, measured from the car´s center line. These values result from the goal of having minimal to no interaction between domain walls and the simulated object. The target is to keep the blockage (Frontal area of the vehicle / Frontal area of the domain) lower than 5 % [19]. The frontal area of the EDGE 14 is about 1.19 m^2, so with the above domain dimensions a blockage of 2.1 % is achieved. As the car is symmetric across its center line, only half of the car is simulated in order to save calculation time and resources. The full domain with the EDGE 14 inside can be viewed in Figure 2.2.

Figure 2.2 – EDGE 14 inside domain

The fluid domain is then generated by simply subtracting the EDGE 14 volume from the windtunnel domain. The resulting volume is the fluidvolume, where the flow will be calculated.

2.3 Physics Model

In order to calculate the flow around the vehicle, fluid properties, physics models and boundary conditions need to be specified that are suited for the external aerodynamic application. A physics continuum is a collection of models that represent the fluid or solid that is being simulated [10].

2.3.1 Boundary Conditions

Before Boudary Conditions can be set up the regions have to be specified and which physics continuum should be applied within it. Around the vehicle a fluid region is chosen (air) and a second porous region needs to be created to represent the flow through the radiator, which also has an effect on the flow behaviour. After that, the Boundary conditions have to be set up according to the situation that should be simulated. The speed of the flow at the windtunnel inlet has to be specified and should be a reasonable value where the vehicle operates. In Figure 2.3 the vehicle speed over time at a typical Formula Student track can be seen. 15 m/s seems to be a speed at which the vehicle is generally operating.

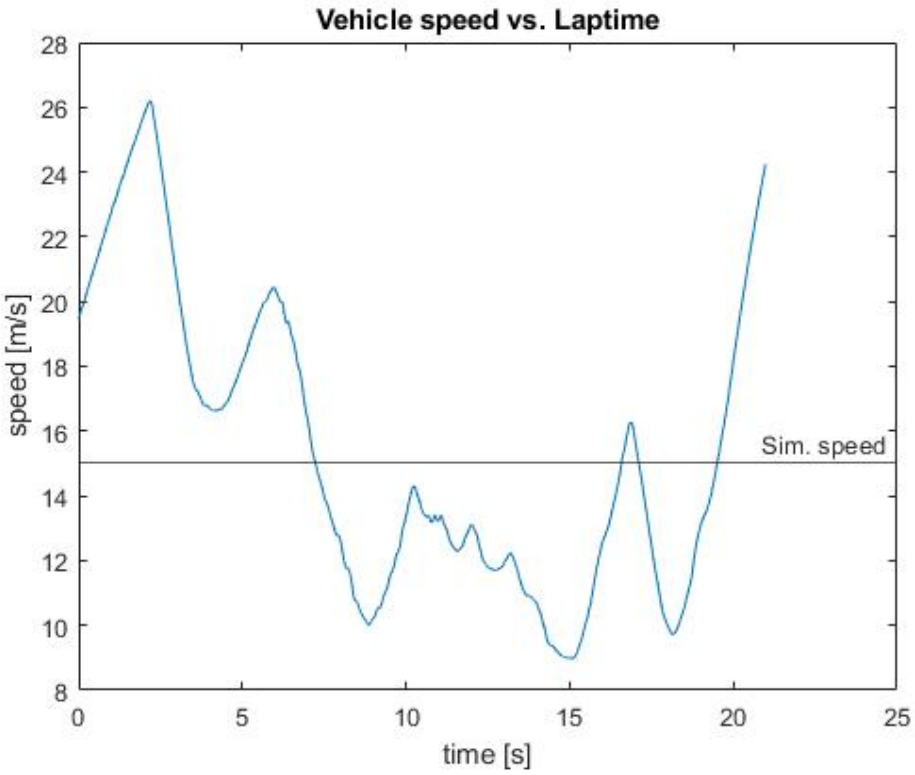

Figure 2.3 – Vehicle speed vs. Laptime

After setting the inlet velocity to 15 m/s, the pressure at the outlet surface is defined as ambient pressure. Furthermore the top, side and floor of the windtunnel are defined as walls and the vehicle center plane is defined as a symmetry plane, as you can see in Figure 2.4.

The inlet velocity of 15 m/s also represents the Initial condition. So when a simulation is started, every Mesh cell is assigned with this speed. Furthermore, it is assumed that the ambient pressure, temperature and density won't change.

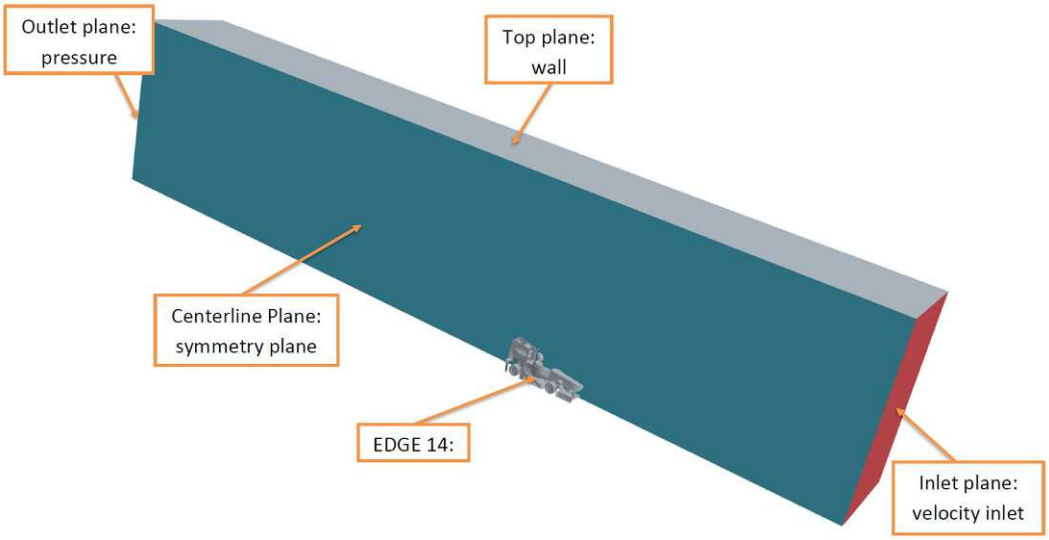

Figure 2.4 – Boundary Conditions

2.3.2 Flow Modelling

As detailed knowledge about the health of the boundary layer is needed, which only arises when we take viscous phenomena into account, this option is chosen in StarCCM+ [22]. As the EDGE 14 is an open wheel vehicle it generates a lot of turbulence, which needs to be modelled correctly and therefore the option turbulent flow is chosen. In Figure 2.3 it can be seen that the vehicle speed never rises above 28 m/s. Therefore the Ma number is way smaller than 0.3 and the flow can be considered incompressible [7]. To keep computation time low, steady state flow is selected. For comparing designs this approach is standard. If the absolute drag and downforce values want to be computed, then time dependency plays a huge role and has to be taken into account. As the EDGE 14 is a three dimensional object, a three dimensional computation needs to be selected. To solve the conservation equations of mass and momentum, StarCCM+ offers the choice between the Segregated Flow and Coupled Flow model. The CPU time scales linearly with cell count, which is unfavourable in this case as the cell count is rather high. The Segregated Flow solver solves the conservation equations in a sequential, uncoupled manner and is applicable for compressible flow. Therefore this model is chosen in combination with a 2nd-Order convection scheme to compute the flux on a cell face in transport equations. This scheme was chosen because of the good accuracy of results.[10]

2.3.3 Turbulence Modelling

Most flows of engineering significance are turbulent and only laminar flows can be completely described by momentum conservation and mass conservation equations. A turbulent condition arises from small disturbances in the flow and can cause a chaotic and random state of motion as you can see from the velocity plot in Figure 2.5. The start of this phenomenon depends on the ratio of inertia force to viscous force, which is otherwise known as the Reynolds number. As shown in Figure 2.5, these fluctuations are impossible to predict. That is why the velocity is being decomposed into a steady mean value $\overline{u}$ and a fluctuating component u'(t).[25]

This decomposition is the basis of the Reynolds-averaged Navier-Stokes (RANS)

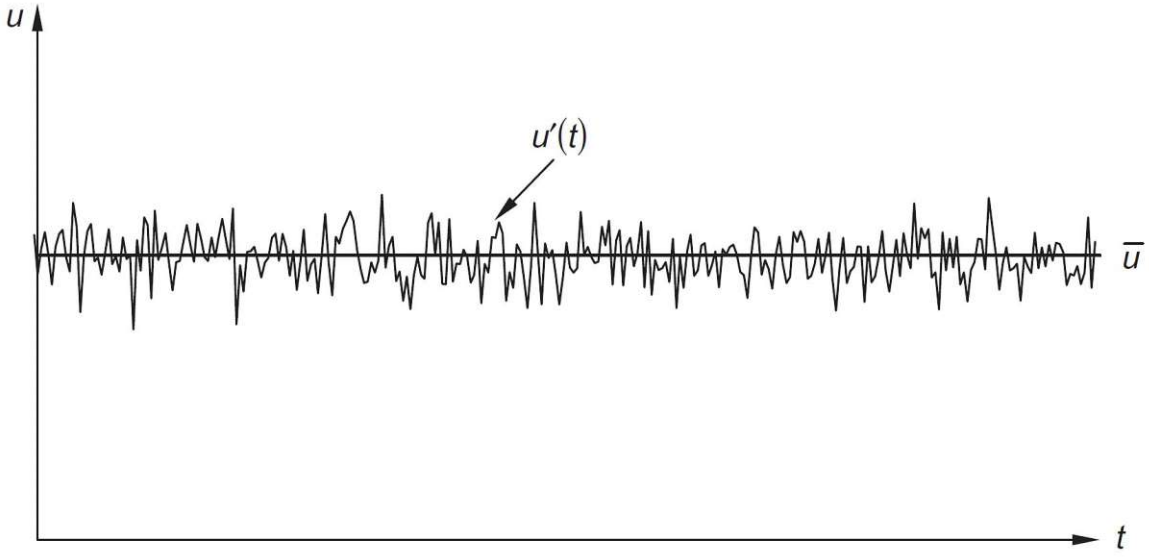

Figure 2.5 – Velocity fluctuation in a turbulent flow, source: [25]

approach. When inserting the mean value and fluctuating component into the Navier-Stokes equations, continuity and conservation equations, the RANS equations result. Only the mean flow is solved and all scales of the turbulence are approximated, furthermore additional independent unknowns are generated because of the averaging process. These are called Reynolds stresses for the momentum equations and act for the influence of turbulence. As a consequence, a turbulence model is needed in order to get closure and be able to calculate the flow characteristics. There are first-order closure (Reynolds stress) or second-order closure models.[4]

The earliest successful form of two-equation turbulence modelling is the k-ϵ model [5],

where k denotes the turbulent kinetic energy and ϵ its dissipation rate [18]. Another two-equation model is the k-ω model, where the dissipation rate is replaced by the frequency of large eddies ω [7]. As the k-ω model is better suited for near-wall flow and the k-ϵ model for freestream flow, Menter combined the two models in the so-called shear-stress transport (SST) model or Menter's [6] model [25]. These are exactly the applications needed for external Aerodynamics where we need to know not only the condition of the Boundary layer (k-ω model) but also want knowledge about the flow far away from the wall (k-ϵ model), so the k-ω SST model is chosen.

2.4 Discretization Method

The discretization of the fluid volume is done using the Finite volume method. The domain is split into a finite amount of very small elements where conservation of mass, impulse and energy have to be fulfilled [3]. The values of the conserved properties are calculated at the centroid of each volume element and then they are interpolated between neighbour cells [25].

These cells form the so-called mesh, which StarCCM+ generates automatically after specifying size and refinement areas. Three mesh types are offered: Polyhedral Mesher, Tetrahedral Mesher and the Trimmed Cell Mesher. As the flow will be mostly aligned along the x-axis, the Trimmed Cell Mesher will be the best option as it is a so-called body-fitted structured Mesh, which is optimal for this application. The size of the mesh cells is controlled with the base size. This specifies the length of a cell and can easily be adjusted if changes to the cell size are needed. Every mesh refinement area is defined as a percentage of the base size, as you can see in Figure 2.6.

One of the most important aspects when designing Aerodynamic elements is the knowledge about the boundary layer of Airfoils. If the boundary layer separates from the Airfoil, then the wing stalls and does not produce any lift (or Downforce in this case). Additionally, it causes a rise in drag, which is another negative aspect. That is why the boundary layer has to be properly resolved. In addition, the point of separation is a very important information used for the next design iteration. A typical boundary layer and its sublayers can be seen in Figure 2.7.

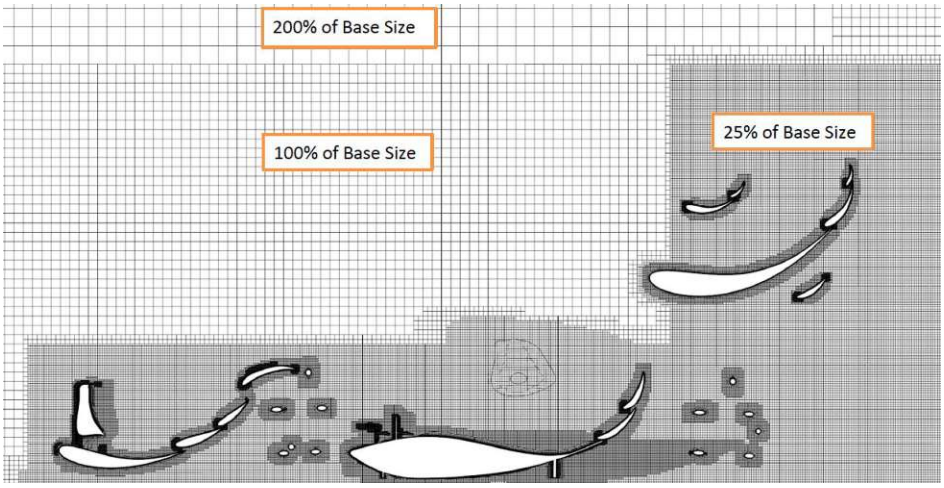

Figure 2.6 – Mesh displayed on a plane through the car

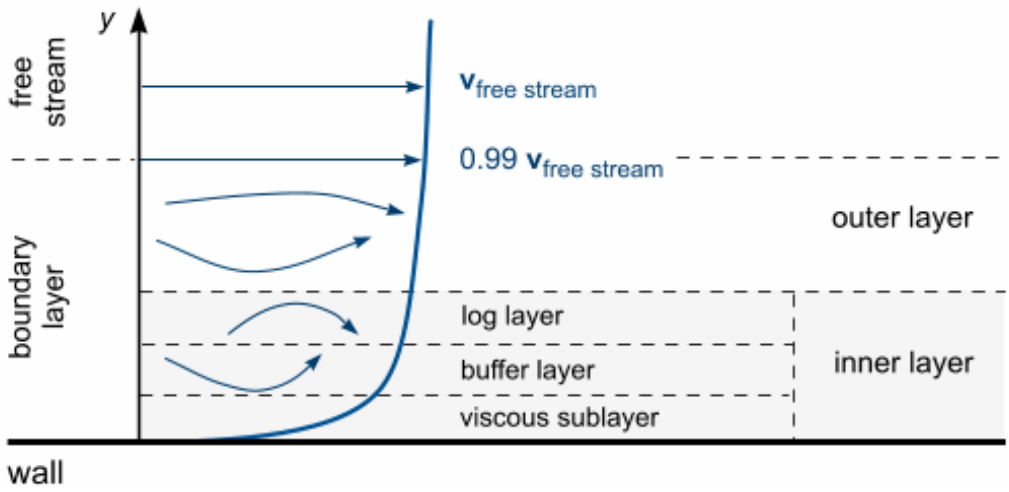

Figure 2.7 – Velocity profile of a turbulent Boundary Layer, source: [10]

In the viscous sublayer, the flow is basically laminar and, according to Direct Numerical simulation and experiments, the velocity component varies linearly with the wall distance [7]. The correlation can be seen in Figure 2.8.

As indicated in Figure 2.8, until a y_+ value of 1-2 there is no difference between DNS (Direct numerical simulation) and the Standard Wall Function for the viscous sublayer. If the dimensionless wall distance is greater than 30, a logarithmic method approaches the exact solution best. If the first cell is located in the logarithmic layer, the computational effort is substantially reduced as less cells are needed and the relationship between velocity and wall shear stress can be derived [7].

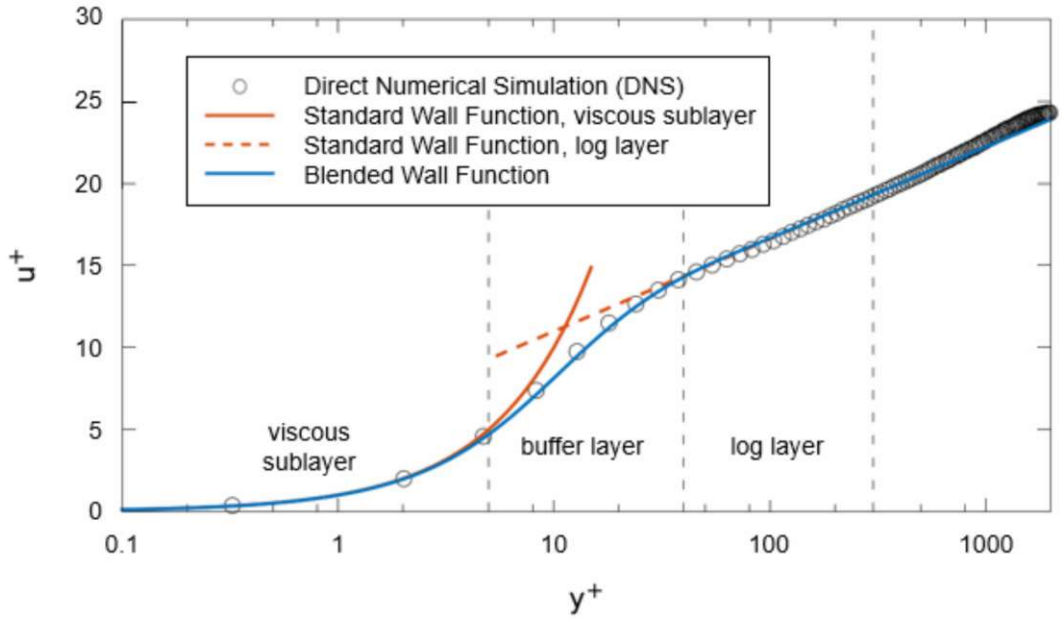

Figure 2.8 – Wall function, source: [10]

2.4.1 High y_+ Approach

For Bodywork parts as the suspension cover, it is enough to take a High y_+ approach (logarithmic approach). In order to resolve the Boundary layer properly, the first cell needs to be at a y+ value of 30 to 100. The Mesh cells used to calculate the Boundary layer are way smaller than regular cells and are so-called Inflation layers. The CFD Software needs the total thickness of the prism layers and the number of prism layers that should be generated. For the high y_+ approach usually 4 prism layers are enough and for the calculation of the total thickness we need the Reynolds number:

$$Re = \frac{Lu_\infty}{\nu} \tag{2.1}$$

The characteristic length of the suspension cover is 836 mm and the far field velocity u_∞ is, as earlier discussed, 15 m/s. The kinematic viscosity of air is 1.51111*10^{-5} $\frac{m^2}{s}$ and the density is 1.225 $\frac{kg}{m^3}$. With these values the Reynoldsnumber is 8.299*10^5, therefore the turbulent regime has to be applied. With this information, the height of the Boundary layer can be calculated using the formula for a turbulent boundary layer on a smooth flat plate aligned parallel to a uniform stream [26]:

$$\delta_{99} = \frac{0.38L}{Re^{0.2}} \tag{2.2}$$

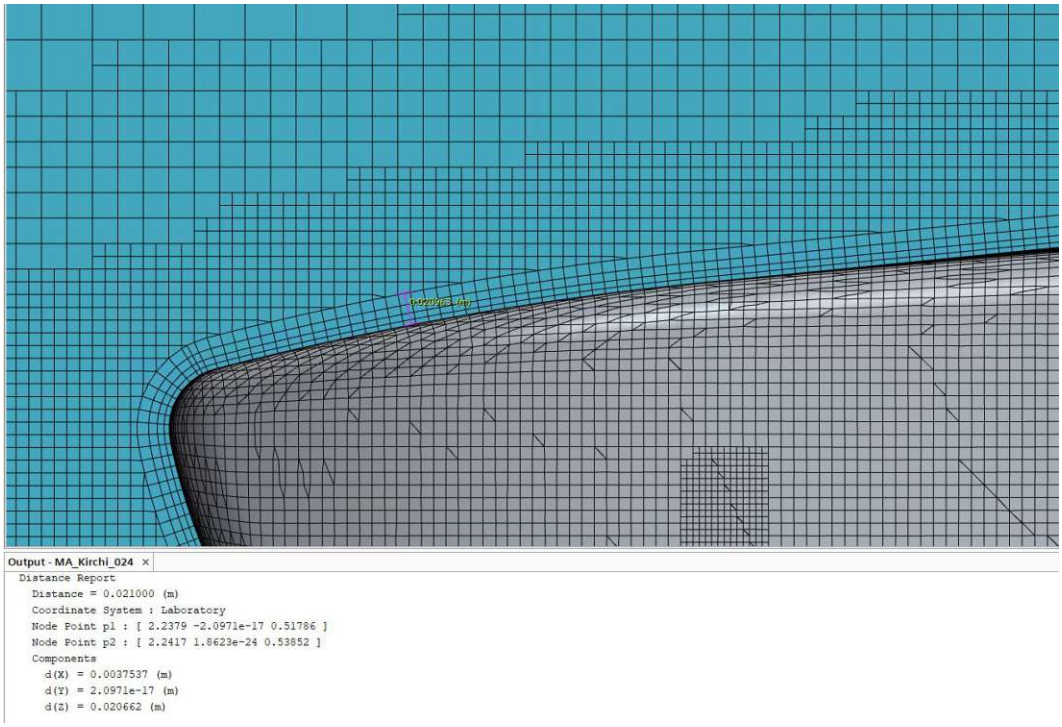

Figure 2.9 – Inflation layers on nose and suspension cover

As you can see in Figure 2.9 there are 4 inflation layers with a total thickness of 21 mm, as specified. After the simulation is finished the y_+ value at this surface needs to be checked if it is inside the logarithmic area ($30 < y_+ < 200$). The resulting wall y_+ value

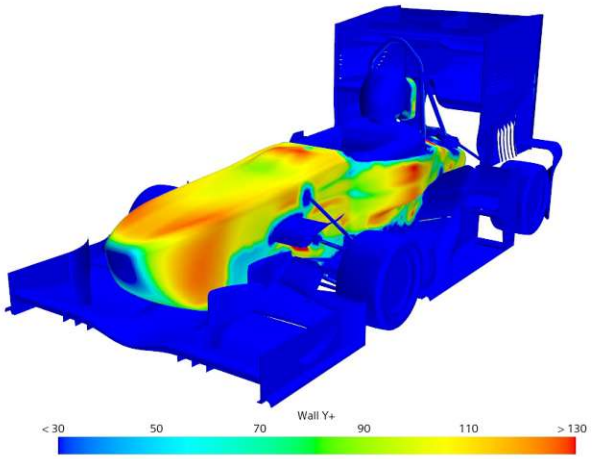

Figure 2.10 – High wall y_+ of suspension cover

on the surface of the suspension cover can be viewed in Figure 2.10. It is everywhere at the suspension cover above 30, and therefore satisfies the requirements.

2.4.2 Low y_+ Approach

If we want to resolve the viscous sublayer, then the Low y_+ Approach is the way to go. This needs to be done on all critical aerodynamic surfaces because otherwise flow separations could occur in reality but not be displayed in the simulation results. For the Mesh generation, knowledge about the height of the first cell, the amount of inflation layers and the growth factor of these layers need to be specified. The calculation of these values will be done for the frontwing flap 2 which has a chord length of 137 mm. With this knowledge the first thing to calculate is the Reynolds number:

$$Re = \frac{Lu_\infty}{\nu} \tag{2.3}$$

The far field velocity u_∞ is, as earlier discussed, 15 m/s. The resulting Reynolds number is 1.35*10^5, therefore the turbulent regime has to be applied. The friction coefficient is calculated like this [20]:

$$c_f = 2 * \left(\frac{0.41}{ln\,(Re)} G\,(ln\,(Re)) \right)^2 \tag{2.4}$$

If the above Reynolds number is used and G(ln(Re)) approximated as 1.5, according to [20], a Friction coefficient of 0.005 results. In order to get the wall shear stress the following equation is used [20]:

$$\tau_w = \frac{1}{2} \rho u_\infty^2 c_f \tag{2.5}$$

After applying the values from above a wall shear stress of $0.689 \frac{N}{m^2}$ results. The following linkage results in the wall velocity or also called sliding speed [7]:

$$u_t = \sqrt{\frac{\tau_w}{\rho}} \tag{2.6}$$

With this velocity of 0.75 m/s, we can compute the necessary wall distance y_p in order to get the desired y_+ of 1. With this dimensionless wall distance the velocity profile is well resolved, even in the viscous and buffer layers [16]. The Formula for the wall distance y_+ can also be found in [7]:

$$y_p = \frac{y_+ \nu}{u_t} \tag{2.7}$$

This would be the distance of the wall to the first computational point. As the computation point of the used cells is in the middle, this distance has to be doubled because StarCCM+ needs the absolute height of the first cell, which results in 0.04 mm. In order to resolve the rest of the boundary layer, the amount of inflation layers and the Growth Ratio normal to the wall needs to be specified. In aerodynamics, the amount of inflation layers is typically between 5 and 30, so 16 layers were sufficient to resolve the boundary layer [1]. A growth factor of 1.3 is chosen and with the knowledge of the prism layer thickness it can be calculated whether these inputs resolve the boundary layer properly.

$$\delta_{99} = \frac{0.38L}{Re^{0.2}} \tag{2.8}$$

A total prism layer thickness of 4.9mm results if we assume the flap surface as a smooth flat plate. After that, the linkage between first cell height, growth factor, amount of inflation layers and boundary layer thickness is used to see if these inputs result in the calculated first cell height.

$$\delta_{99} = \sum_{i=1}^{N} \frac{y}{2} * r^{i-1} \tag{2.9}$$

With the usage of a numerical solver, a value for the absolute first cell height of 0.045 mm results. The outcome only deviates 0.005 mm, so the mesh can be generated. After the simulation computation is complete, the resulting wall y_+ values need to be checked.

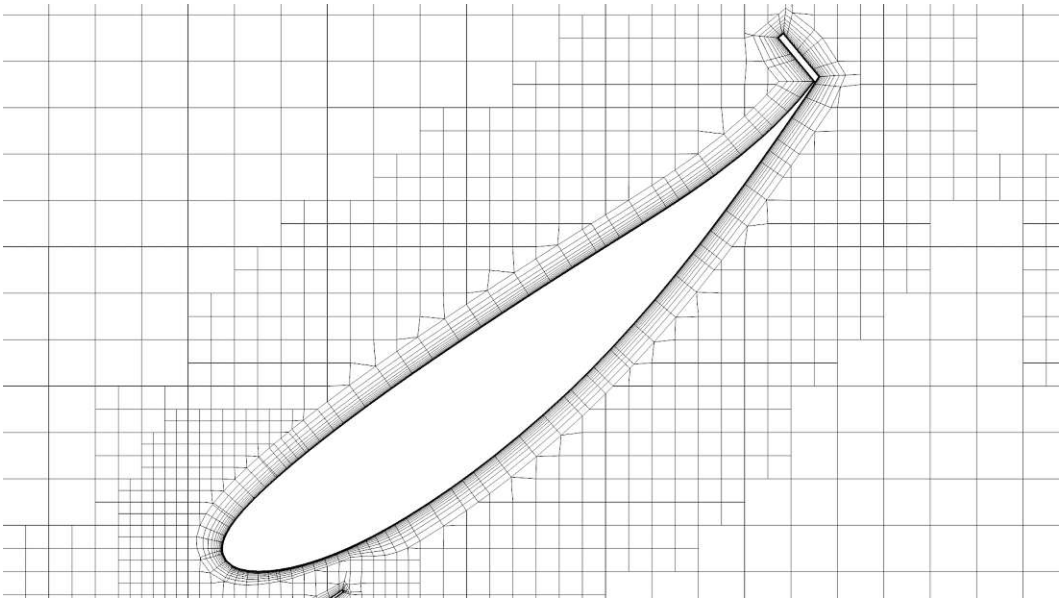

Figure 2.11 – Inflation layers around frontwing flap 2

The resulting mesh with the inputs: prism layer total thickness equals 5 mm, 16 inflation layers and a growth factor of 1.3 is displayed in Figure 2.11. After the simulation

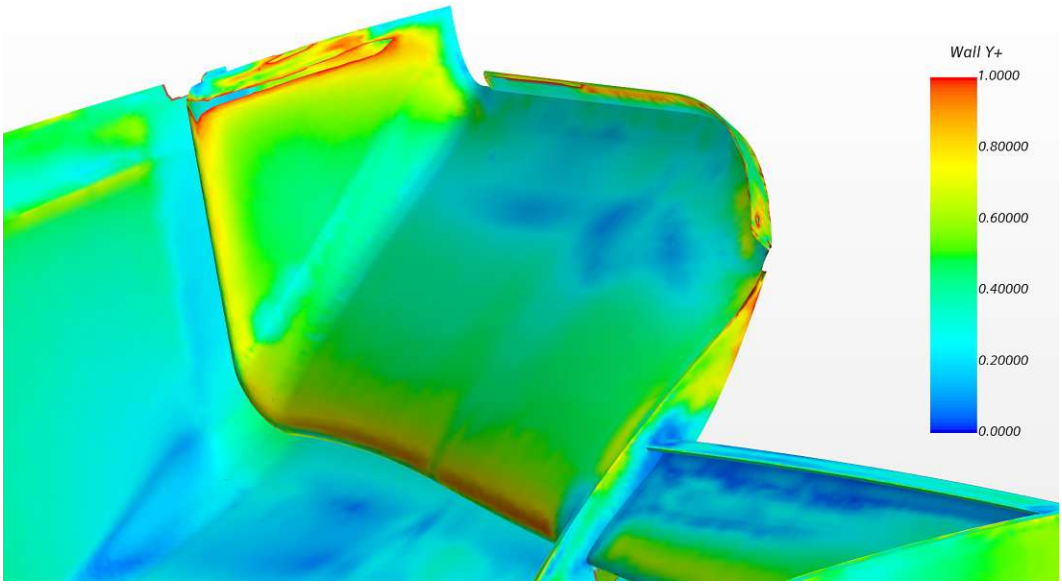

Figure 2.12 – Low wall y_+ of frontwing flap 2

computation is finished the mesh inputs can be checked by looking at the dimensionless wall distance values. Figure 2.12 shows that the desired value of 1 is not exceeded and therefore satisfies the requirements of a proper boundary layer resolution.

2.4.3 Mesh Refinement study

As we are not able to use an infinitely small mesh which represents the reality, there will always be a discretization error. This error has to be kept at a minimal level because it is important to know the aerodynamic forces acting upon the surface in order to design them structural stiff enough to withstand the maximum loads. For example, when refining the mesh of the undertray, the generated downforce rises because small eddies are resolved better than with a coarse mesh. By comparing systematically refined meshes, the discretization error can be calculated [7]. This is done with a Richardson Extrapolation, where three significantly different sets of grids have to be generated and the refinement factor should vary more than 1.3 [15]. As a representative cell length the base size, as explained earlier, is chosen and simulations with different meshes are run. The results obtained can be seen in Figure 2.13.

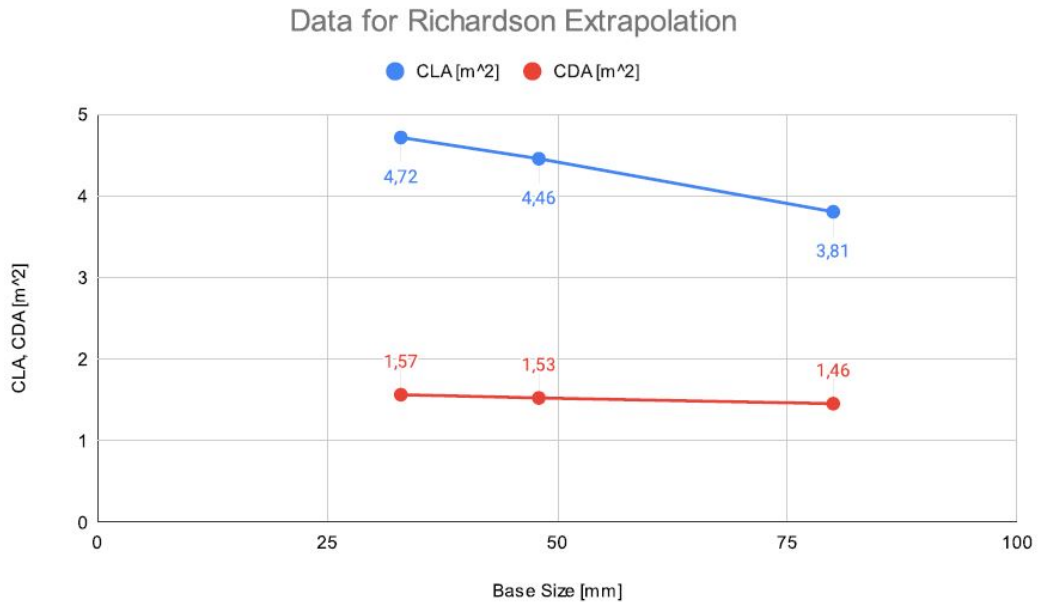

Figure 2.13 – Simulation results with 3 different Meshes

As Figure 2.13 sows, the simulation results depend a lot on the size of the used mesh. To calculate the Grid Convergence Index, the order p of the method has to be calculated first. All expressions used for the Richardson Extrapolation can be found in [15].

$$r_{21} = \frac{h_2}{h_1} \tag{2.10}$$

$$r_{32} = \frac{h_3}{h_2} \tag{2.11}$$

$$\varepsilon_{21} = \phi_2 - \phi_1 \tag{2.12}$$

$$\varepsilon_{32} = \phi_3 - \phi_2 \tag{2.13}$$

$$p = \frac{1}{\ln r_{21}} \mid \ln \mid \frac{\varepsilon_{32}}{\varepsilon_{21}} \mid + q(p) \mid \tag{2.14}$$

$$q(p) = \ln\left(\frac{r_{21}^p - s}{r_{32}^p - s}\right) \tag{2.15}$$

$$s = 1 * sgn\left(\frac{\varepsilon_{32}}{\varepsilon_{21}}\right) \tag{2.16}$$

Equations 2.14, 2.15 and 2.16 are coupled and can be solved using fixed-point iteration [15]. The calculated conversion index p for CLA is 1.3. A higher order of convergence is closer to the exact solution (mesh size = infinitely small) and should ideally be at 2 [2]. With the knowledge of the conversion index, the exact solution can be calculated using this expression:

$$\phi_{ext}^{21} = (r_{21}^{p}\phi_1 - \phi_2)/(r_{21}^{p} - 1) \tag{2.17}$$

This results in a CLA of 5.15, so mesh independence at a base size of 33 mm has not been achieved as there is still a big difference to the exact solution. In order to investigate how fine the mesh needs to be to represent the exact solution, further simulations with finer mesh settings are carried out.

Base Size [mm]	Cell count [Mio. cells]	CLA[m^2]	CDA[m^2]
80	10	3.81	1.46
48	19	4.46	1.53
33	34	4.72	1.57
26	55	4.95	1.61
22	79	5.04	1.67
20	98	5.1	1.68
18	124	5.21	1.72
16	163	5.2	1.71

Table 2.1 – Change of CLA and CDA due to mesh refinement

As you can see in Table 2.1, the cell amount rises very fast when reducing the base size and at some point the computing power is not sufficient enough to generate more cells. The Base Size of 16 mm is the finest Mesh possible to produce with the available workstations at TU Wien Racing and it can be seen, that the values stagnate at the two finest meshes. The extrapolated CLA value of 5.15 is very close to the independent solution of 5.2. So in order to keep the discretization error at a Minimum and be independent of the mesh, at least a base size of 18 mm needs to be applied, as you can see in Figure 2.14. In the design phase this is not possible because the runtime is 4 times higher than with the usual Base Size of 33 mm.

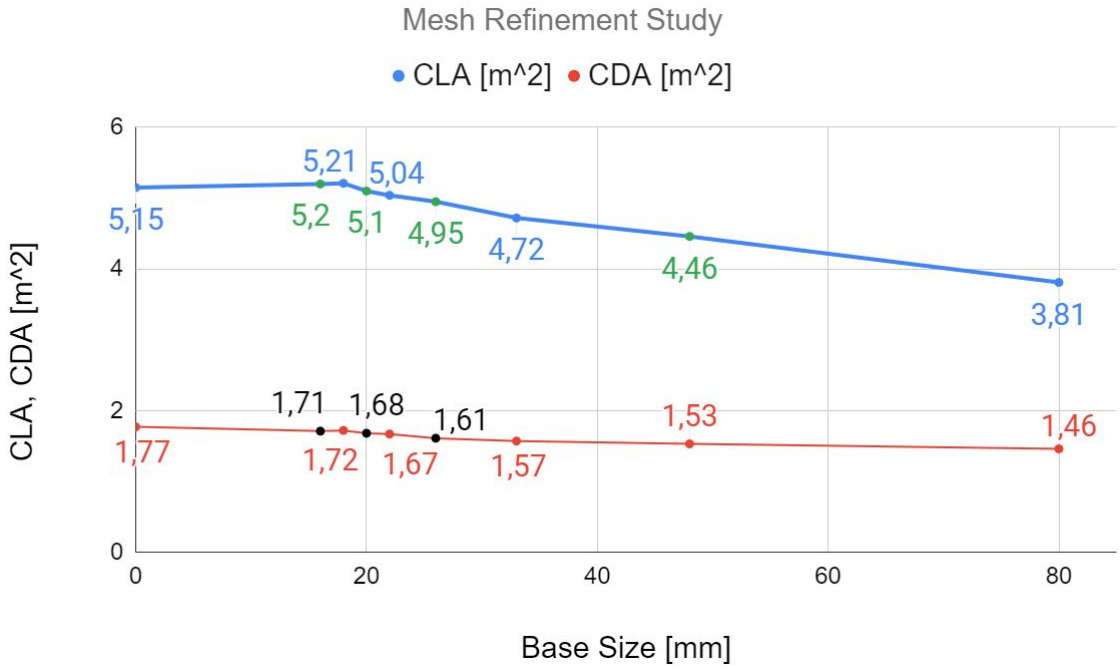

Figure 2.14 – Visualisation of Mesh Refinement Study

To get the Grid Convergence Index (GCI), the approximate relative error has to be calculated first, according to [15]:

$$e_a^{21} = \left| \frac{\phi_1 - \phi_2}{phi_1} \right| \tag{2.18}$$

The extrapolated relative error for the CLA value is 5.51% and has been calculated with this expression [15]:

$$e_{ext}^{21} = \left| \frac{\phi_{ext}^{12} - \phi_1}{\phi_{ext}^{12}} \right| \tag{2.19}$$

In order to get the fine-grid convergence Index the following correlation can be applied [15]:

$$GCI_{fine}^{21} = \frac{1.25 e_a^{21}}{r_{21}^p - 1} \tag{2.20}$$

With expression 2.20 it can be concluded that the numerical uncertainty of the grid for the CLA value is 11.33%. All the results of the Richardson Extrapolation for CLA and CDA can be viewed in the table below (Table 2.2).

	ϕ=CLA[m^2]	ϕ=CDA[m^2]
N_1,N_2,N_3	10*10^6,19*10^6,34*10^6	10*10^6,19*10^6,34*10^6
r_{21}	1.44	1.44
r_{32}	1.67	1.67
ϕ_1	4.72	1.57
ϕ_2	4.46	1.53
ϕ_3	3.81	1.46
p	1.3	0.51
ϕ_{ext}^{21}	5.15	1.77
e_a^{21}	5.51%	2.55%
e_{ext}^{21}	8.31%	11.19%
GCI_{fine}^{21}	11.33%	15.74%

Table 2.2 – Calculation of the discretization error for CLA and CDA

2.5 Convergence Criteria

As the solution is generated using an iterative approach, a criteria has to be specified when the solution is converged (the error between two iterations approaches 0) and the iteration process should stop [7]. This stopping criteria can be specified by maximum iteration steps or when a certain value (for example CLA or CDA) does not change more than a specified value from one iteration to another. In a steady-state simulation, as used in this application, the maximum iteration steps are specified. At 1800 iterations the solution is usually converged as showcased in Figure 2.15.

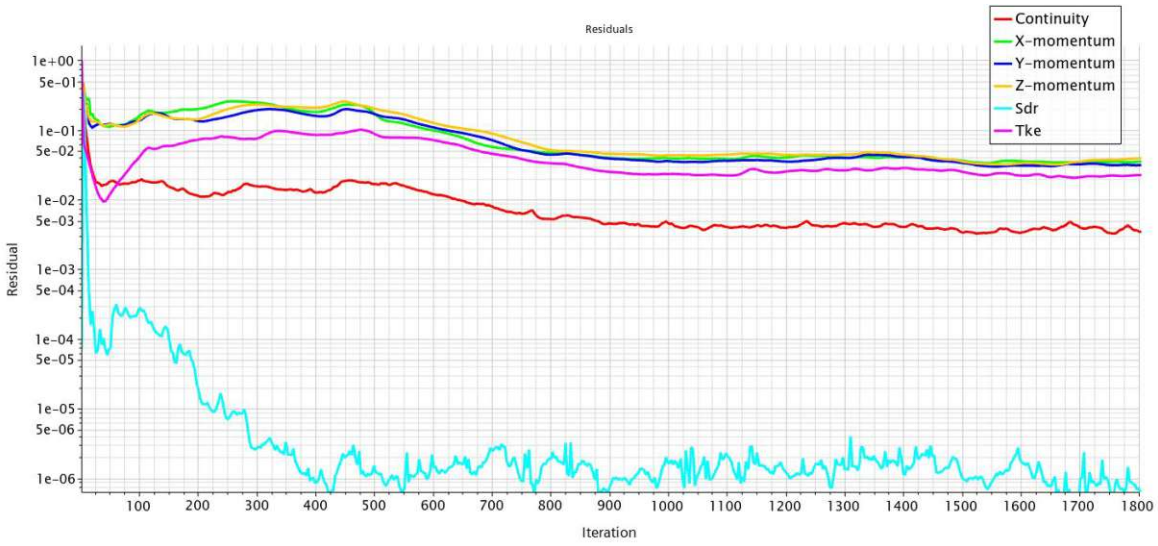

Figure 2.15 – Residuals after 1800 iterations

To be sure that nothing significant changes after 1800 iterations, 10000 iterations have been completed (Figure 2.16).

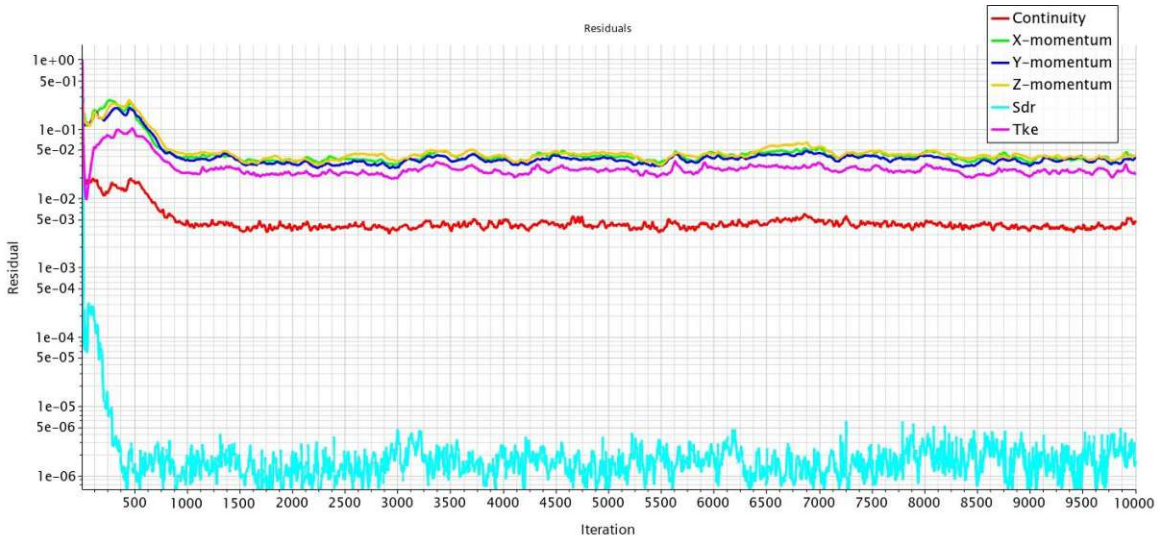

Figure 2.16 – Residuals after 10.000 iterations

The difference between the residuals can be found in Table 2.3.

Residual	1800 Iterations	10000 Iterations	Relative difference [%]
Continuity	0.0035	0.0045	22.2
X-momentum	0.034	0.0412	17.4
Y-momentum	0.031	0.0414	25.1
Z-momentum	0.039	0.0413	5.6
Sdr	$7.199*10^{-7}$	$1.57*10^{-6}$	54.1
Tke	0.0227	0.0221	2.7
CDA	1.57	1.51	3.9
CLA	-4.66	-4.66	0

Table 2.3 – Comparison of Residuals, CDA and CLA at 1800 iterations and 10000 iterations

3

Validation

The last part of the CFD simulation process is verification and validation. It is vital to know if the simulated results resemble the reality and if the CFD results are accurate enough. For verification and validation studies, high-quality full-scale or reduced-scale measurements with enough accuracy have to be carried out [4]. Verification deals with the correct setup of a CFD simulation in terms of correct boundary conditions, equations and parameter values, while validation is the process of assessing the accuracy of the results and comparing these with experimental measurements [2]. Concerning verification purposes it is enough to check if the solution is physically correct (for example looking at the velocity plots from inlet to outlet) or asking an experienced CFD engineer to check the solution. Validation can be carried out using Direct Numerical Simulation (DNS) and comparing these results to, for example, results obtained from RANS simulations. In this case this is not possible as the computational power required to simulate the EDGE 14 vehicle is not affordable. The following chapters will focus on different ways of experimental validation.

3.1 Aero Rake

A popular way in Motorsport to assess the quality of CFD results is to use a so-called aero rake which is mounted in a highly turbulent region of the flow around the car and then the measured pressure is compared with the obtained CFD results. Knowing of the pressure magnitude, the speed results and other flow specific properties can be calculated, and therefore this is called the mother of all properties of an airflow [23]. The aero rake used by Red Bull in Formula 1 can be seen in Figure 3.1 and is placed right behind the front tyre. The tyres of open wheel cars are responsible for a majority

of the vehicles drag. That is the reason why the prediction of this highly turbulent zone and everything that follows is very important and needs to be validated.

A similar aero rake has been developed at TU Wien Racing in the process of a Seminar

Figure 3.1 – Aero Rake of Red Bull Racing, source: [13]

thesis [17]. To fit the aero rake onto the undertray behind the front wheel of the EDGE 14, the author designed and 3D printed attachments which were used in combination with two threaded rods to secure the rake at high speeds. The result can be viewed in Figure 3.2.

Figure 3.2 – Aero Rake attached to the EDGE 14

3.1.1 Fundamentals of pressure measurement

It is common practice to measure either the dynamic pressure or the total pressure with Pitot tubes. With a Pitot tube the relative velocity between the vehicle and airflow can be measured as a function of the pressure differences as you can see in Figure 3.3 [24]. Intake a is for measuring the reference (ambient) pressure and intake b measures the

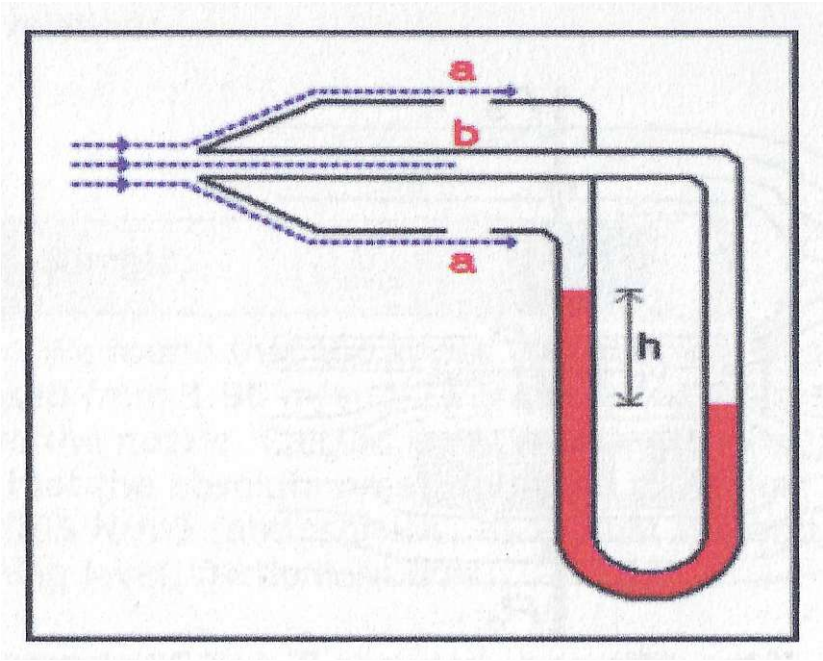

Figure 3.3 – Schematic picture of a Pitot tube, source: [24]

total pressure at the intake. With the knowledge of these 2 pressures and the density it is easy to calculate the velocity.

$$p_t = p_{ref} + \rho v^2 \frac{1}{2} \tag{3.1}$$

In order to get the pressure values, a measuring device is needed which either works differentially to directly output the term $\rho \mathrm{v}^2 \frac{1}{2}$ or absolute. In this case the absolute pressure sensor P8-A (Figure 3.4) by EvoScann is chosen, which is a state of the art sensor also used in Formula 1. As the name suggests, it has got 8 measurement channels which can be connected to the pitot tube with tubes. The accuracy of the measured values is 0.1% of the final sample value of 1200 mbar [11].

Figure 3.4 – Absolute pressure sensor P8-A

Pitot tubes are very sensitive with the angle of attack of the incoming flow, so the stream must be aligned to the tube itself. As the goal is to detect the flow structures in a highly turbulent zone where the flow is not aligned to the pitot tubes on the aero rake, Kiel probes are used. Their onset flow angle acceptance is remarkable and they can measure the correct absolute pressure up to 40 degrees of yaw [8]. They are calibrated in the windtunnel to securely detect the right value and can be viewed in Figure 3.5 already mounted on the aero rake and connected with tubes to the absolute pressure sensor.

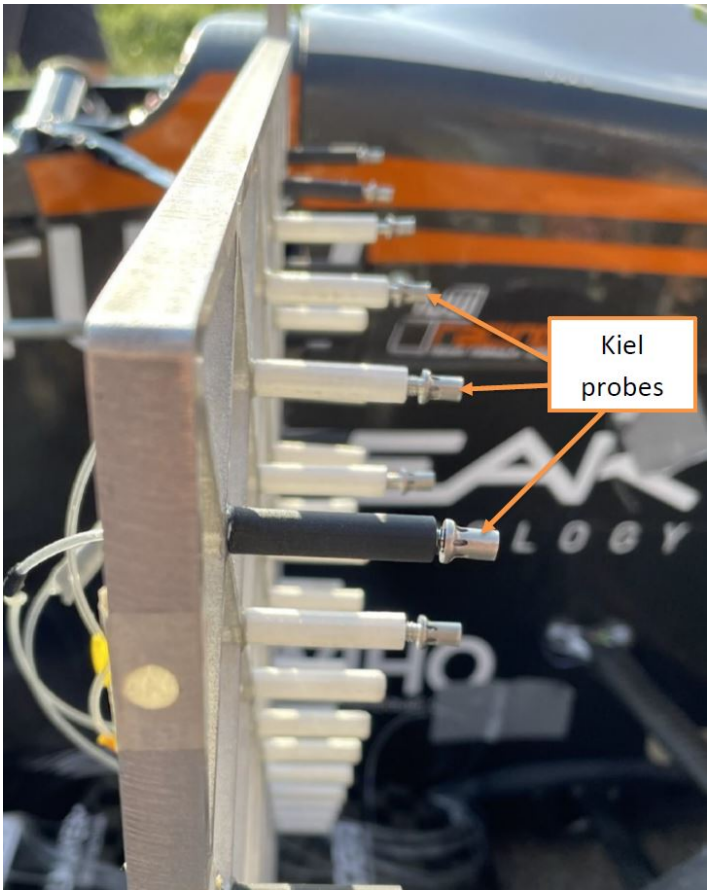

Figure 3.5 – Kiel probes mounted on Aero Rake

3.1.2 Wake Comparison

It is common practice in CFD to look at the wake of bodies with the total pressure coefficient (cpT). That way low energy areas can be identified as a result of aerodynamic devices or wheels. The total pressure coefficient is calculated like this:

$$cpT = \frac{p_t - p_{ref}}{\frac{1}{2}\rho_{ref} v_{ref}^2} \tag{3.2}$$

In order to get the correct velocity value it would be helpful to have a Pitot tube right above the rake as Red Bull does in Figure 3.1. However, as only one pressure scanner with 8 channels is available and 61 measurement points need to be assessed on the rake, it is simpler to take the vehicle speed. If a Pitot tube was used additionally, 2 measurement ports would be permanently taken and so instead of 8 runs for the 61 measurement points, 11 runs would be needed.

The validation procedure starts with assessing the total pressure at 0 m/s and then the vehicle moves along a long straight at constant velocity to get pressure values at a steady state condition. The values at 0 m/s are taken as reference values and the total measurements during straightline are averaged as they are fluctutating a lot as you can see in Figure 3.6.

Figure 3.6 – Speed and total pressure of channel 1 during rake validation

After averaging the total pressure measurements from 11:05:10 to 11:05:25 when the vehicle was not moving, a reference pressure of 994.56 mbar is obtained. During 11:05:53 and 11:06:02 the velocity is assumed constant at 15 m/s and the averaged total pressure is 994.7 mbar.With these measurements and a reference density of 1.225 kg/m^3 the total pressure coefficient results in 0.2. This procedure is done for all 61 measurement points and then inserted to Matlab to obtain the interpolated wake in Figure 3.7. Note that each of the red stars symbols a measurement point.

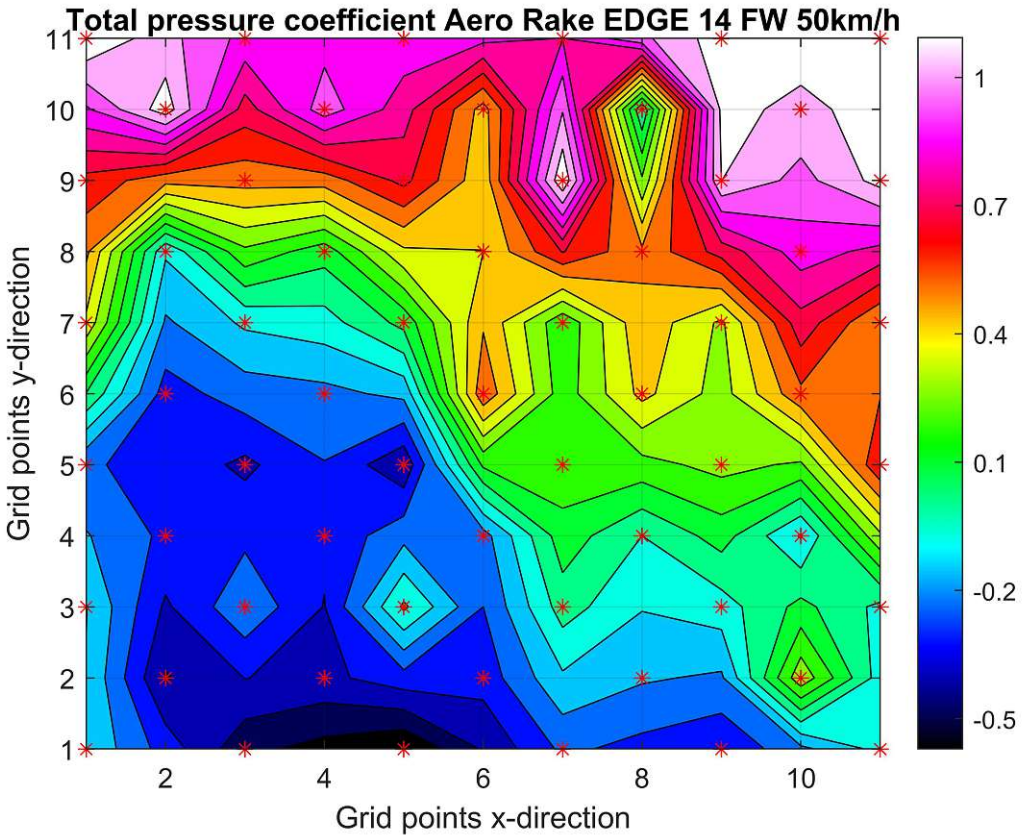

Figure 3.7 – Front Tyre Wake with EDGE 14 frontwing captured with the aero rake

3.1.3 Correlation to CFD results

In order to validate the quality of the CFD simulation, the experimental results obtained in Figure 3.7 have to be compared to the computational results. For that the exactly same situation as during the experimental tests has to be reconstructed in CFD concerning vehicle attitude, geometry and speed. The speed can be obtained from the live telemetry as shown in Figure 3.6. The front and rear ride heights are measured using linear potentiometers attached to the suspension and are also connected to the live telemetry. As you can see in Figure 3.8, during acceleration the springs compress and the vehicle approaches the ground until a steady state is reached at a point of constant velocity. The resulting front ride height of and rear ride height are used to adjust the CAD model in CFD.

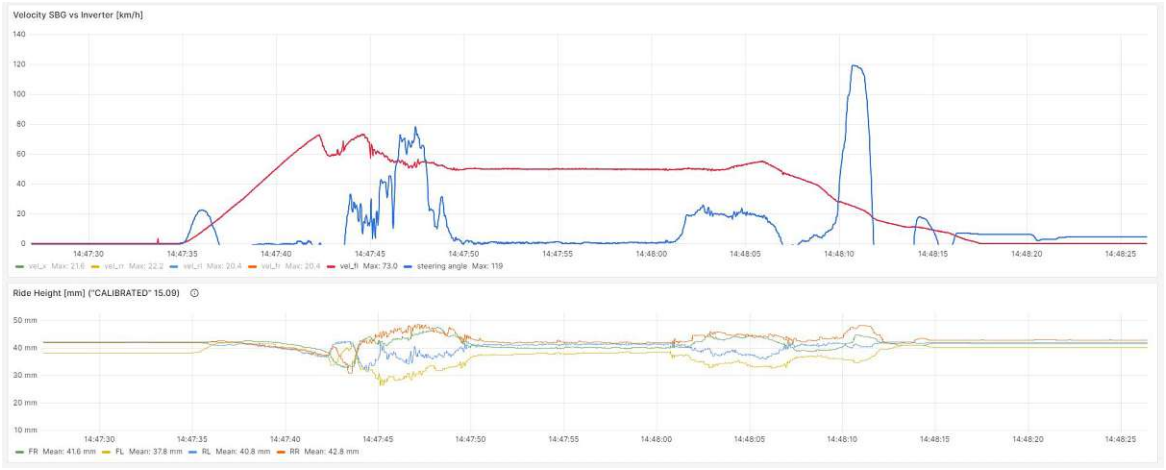

Figure 3.8 – Speed, steering angle and associated front and rear ride heights (left and right)

In order to simulate the same geometry as tested, the aero rake, including all attachments, has to be added to the vehicle model. The obtained solution of the CFD simulation can be viewed in Figure 3.9. Note that it is a straightline halfcar simulation so the results on one side of the car are mirrored to the other side. In reality only one rake is mounted but the influence to the other side is minimal.

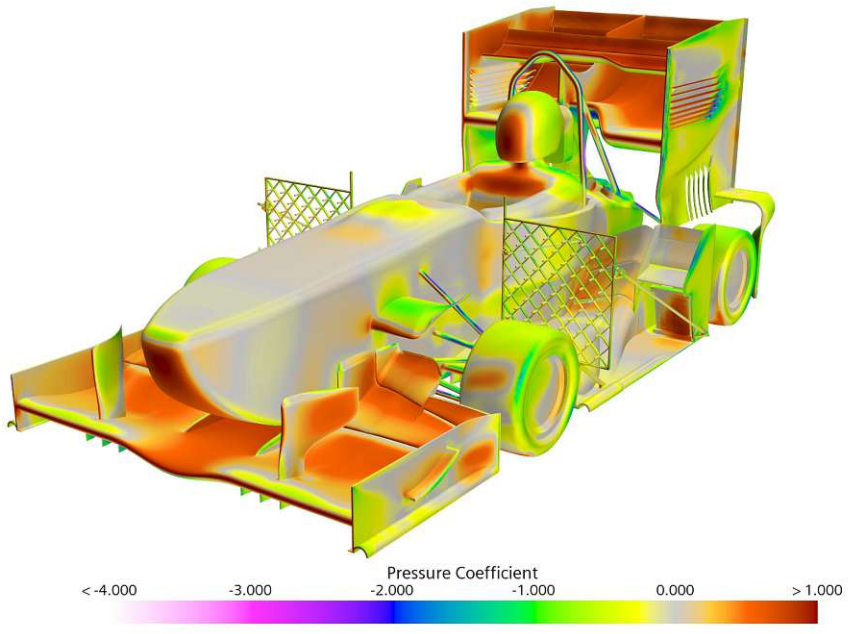

Figure 3.9 – Resulting pressure coefficient with rake

To compare the total pressure coefficients with the experimental results, a new scene is created exactly at the plane through the Kiel probes. The obtained image can be seen in Figure 3.10 and should be compared to the results shown in Figure 3.7. The grey dots resemble the Kiel probes. When comparing the results, it is clearly visible that

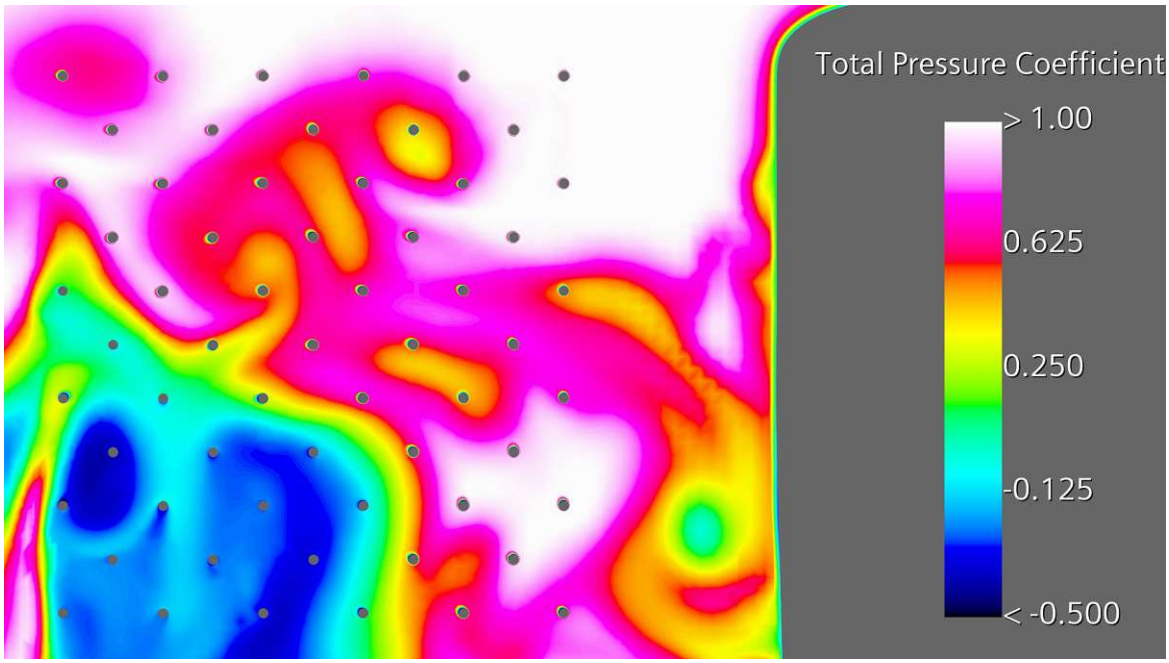

Figure 3.10 – Front tyre wake with EDGE 14 frontwing using CFD

the overall structure is resolved very well but some points vary due to the resolution of the grid or the accuracy of the measurement itself. In order to reduce the error caused by the measurement, another simulation is started where the frestream velocity is not 15 m/s anymore but 22,2 m/s (80 km/h). The result of the total pressure coefficient in the aero rake plane can be viewed in Figure 3.11, and it is clearly visible that the flow structures did not change a lot.

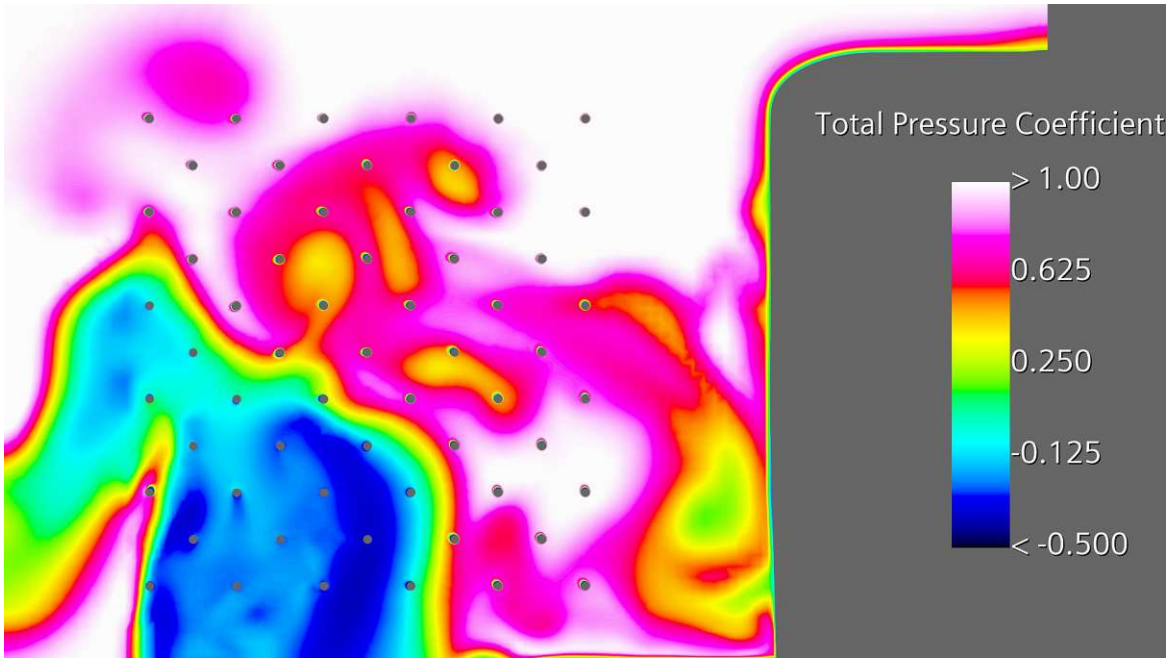

Figure 3.11 – Front tyre wake with EDGE 14 frontwing using CFD at 22,2 m/s

However, when comparing the static pressures at this plane, there are major quantitative differences as you can see in Figure 3.12. With higher velocity, the dynamic pressure also rises and therefore the difference in total pressure between a low pressure zone and a high pressure zone is bigger. Therefore higher velocity runs are more reasonable in terms of measurement accuracy.

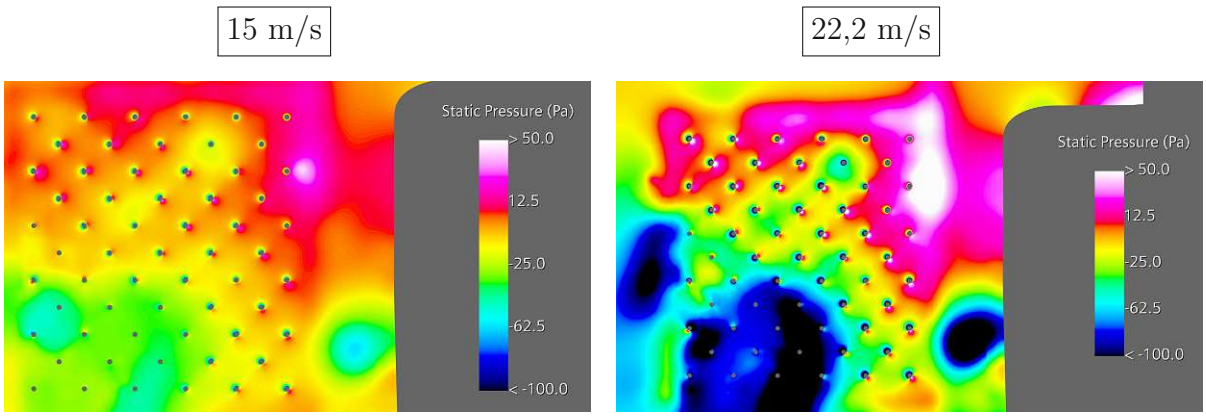

Figure 3.12 – Static pressure comparison at different velocities

All CFD simulations have been conducted as steady-state RANS calculations. In order to investigate the influence of time on the wake of the front tyre, an unsteady RANS simulation has been set up. As you can see in Figure 3.13, only the magnitude of the total pressure coefficient behind the front tyre changes and the placement of a few flow

features moves a little bit. The overall structure and wake, compared to the steady-state solution, is very similar, therefore the steady-state approach is alright in order to save computational ressources.

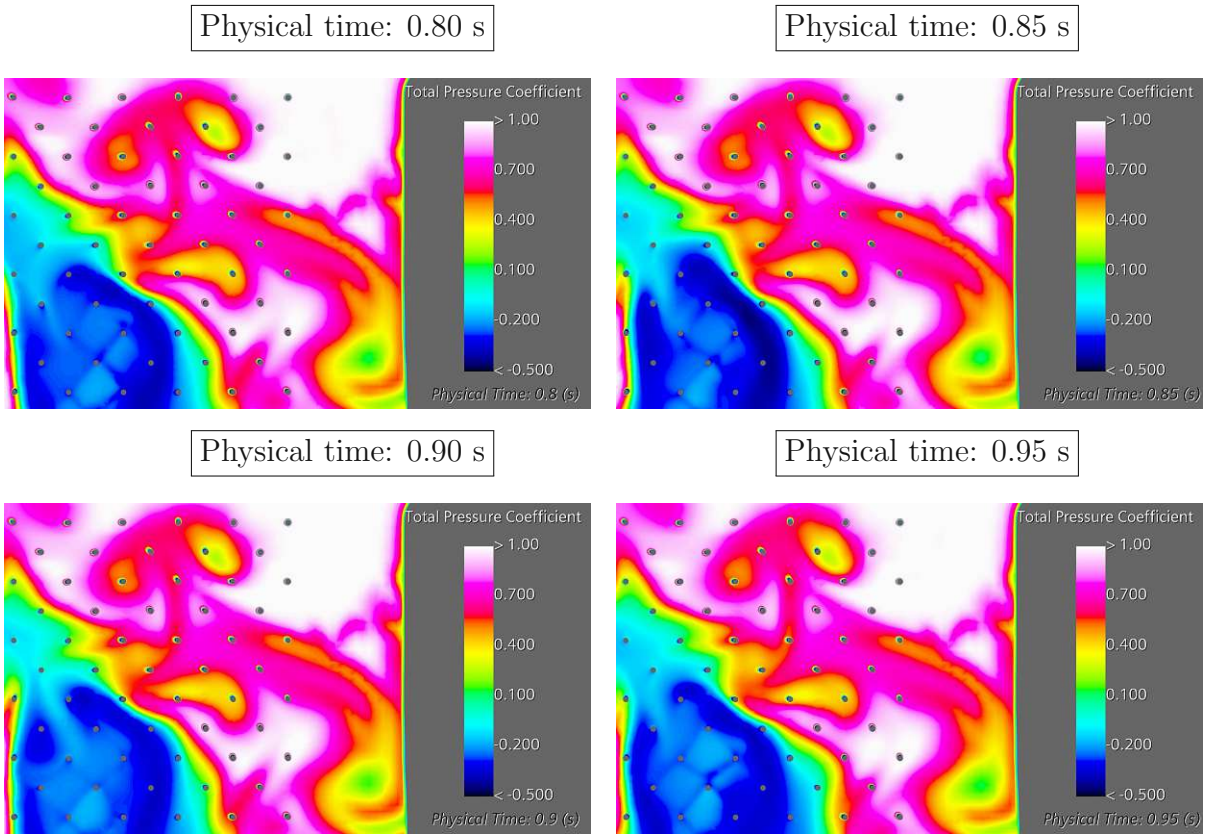

Figure 3.13 – Wake results at different time stamps

3.1.4 Results wake EDGE 14 frontwing with 50 km/h

The comparison of the results obtained with the aero rake and CFD results at 50 km/h can be seen in Figure 3.14. The resulting turbulences of the front tyre are clearly visible. Furthermore, the bullhorn vortex is at the exact position as in the CFD simulation, which confirms the accuracy of the rake mount and the experimental results. The effect of the frontwing turning vane can also be seen, as the top of the front tyre wake is being pushed outboard, just as predicted in the simulation. One characteristic flow feature that is clearly missing is the clean air on the bottom right corner of the rake. This can either be due to faulty measurements or wrong CFD results.

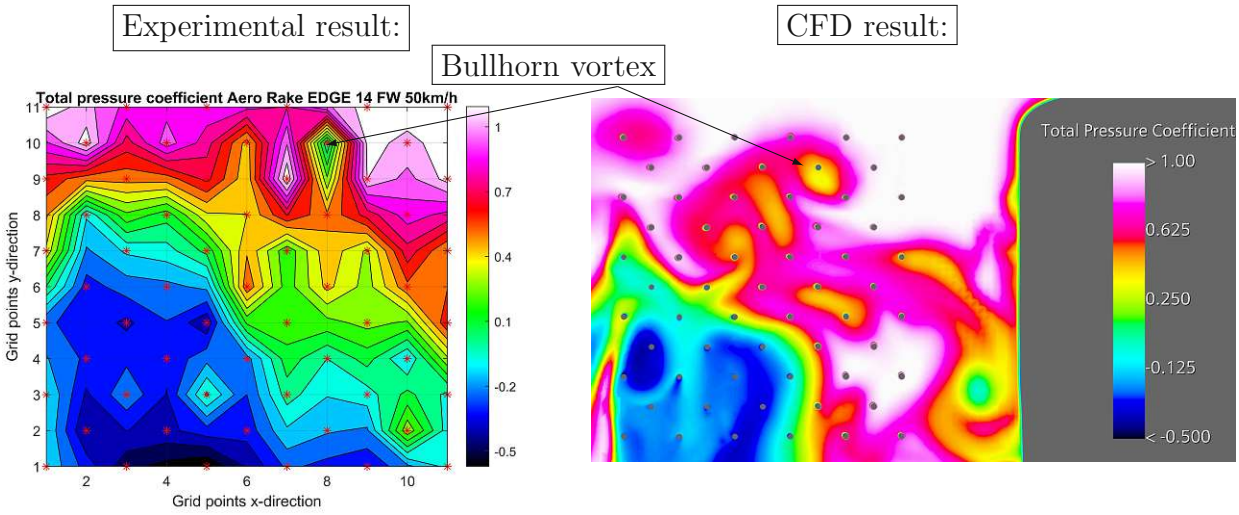

Figure 3.14 – Comparison of experimental rake results and CFD results with the EDGE 14 frontwing at 50 km/h

3.1.5 Results wake EDGE 14 frontwing with 80 km/h

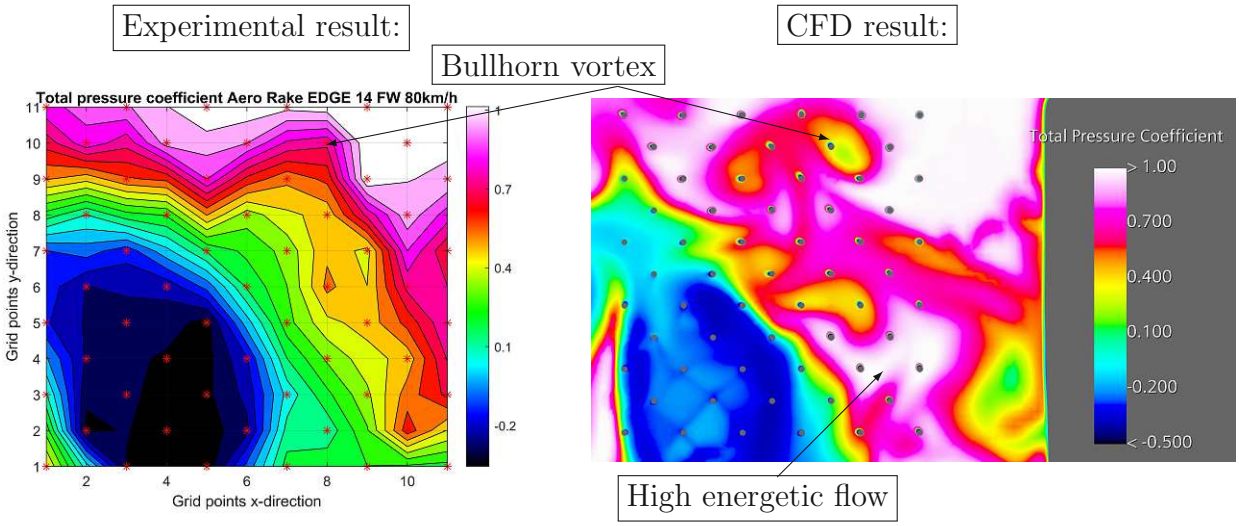

Figure 3.15 – Comparison of experimental rake results and CFD results with the EDGE 14 frontwing at 80 km/h

As you can see in Figure 3.15 the wake of the front tyre is, in terms of position and magnitude of cpT, very well predicted. The transition to turbulent flow on the outside of the tyre is resembled pretty accurate and also the position of the bullhorn vortex matches. However, the region of high energetic flow on the bottom right of the rake is missing again.

3.1.6 Results wake EDGE 13 frontwing with 80 km/h

In order to see results for a different geometry, the frontwing of the EDGE 13 is mounted as you can see in Figure 3.16. This frontwing is significantly different from the EDGE 14 frontwing. There is no turning vane to control the front tyre wake and the structure of the flaps behind the mainfoil is also different.

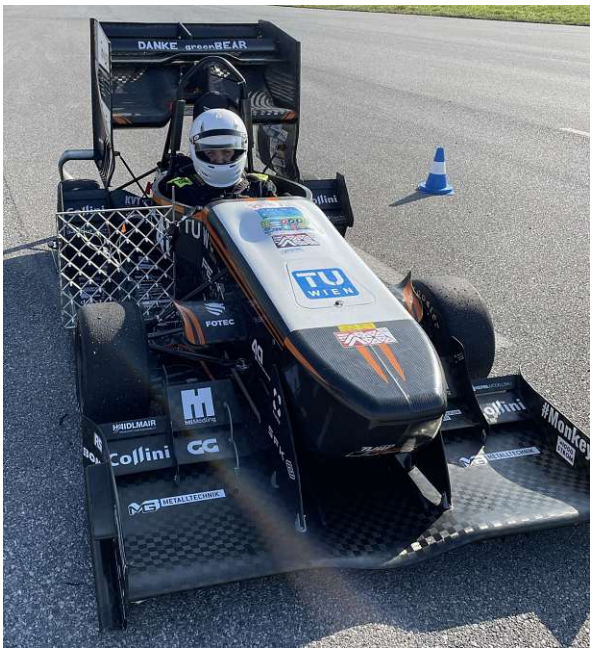

Figure 3.16 – Aero rake in combination with EDGE 13 frontwing

The measurements were carried out with 80 km/h again and the CFD simulation was executed with the vehicle attitudes according to the live telemetry. After viewing the results it is clearly visible that there was a problem with Kiel probe number 6. Three times completely wrong pressure values were measured as you can see in Figure 3.17.

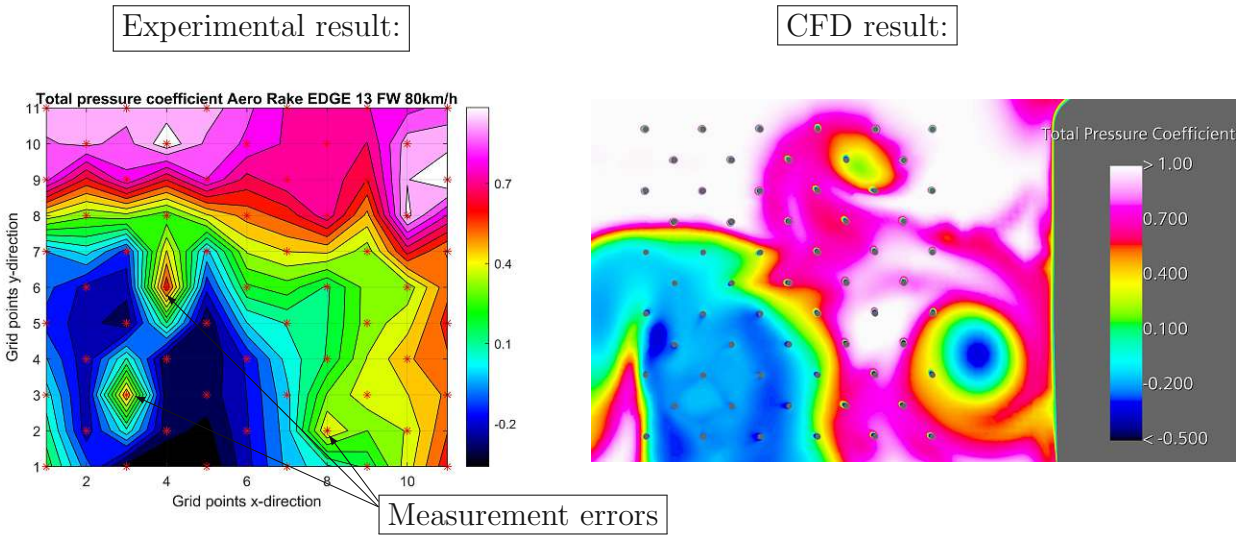

Figure 3.17 – Measurement errors of channel 6

After deleting these 3 measurements, the experimental results and CFD results are matching. It is clearly visible in Figure 3.18 that the transition of turbulent tyre wake and clean high energetic flow above the tyre is predicted pretty well. Furthermore, the end of the turbulent zone on the outside of the tyre can be seen. Unfortunately the aero rake is too far outboard to capture the frontwing tip vortex but the impact of it is also clearly visible. The colorbars of CFD and experimental results are exactly the same. The overall experimental result is more turbulent than the CFD outcome, as there are less white zones which resemble laminar freestream flow.

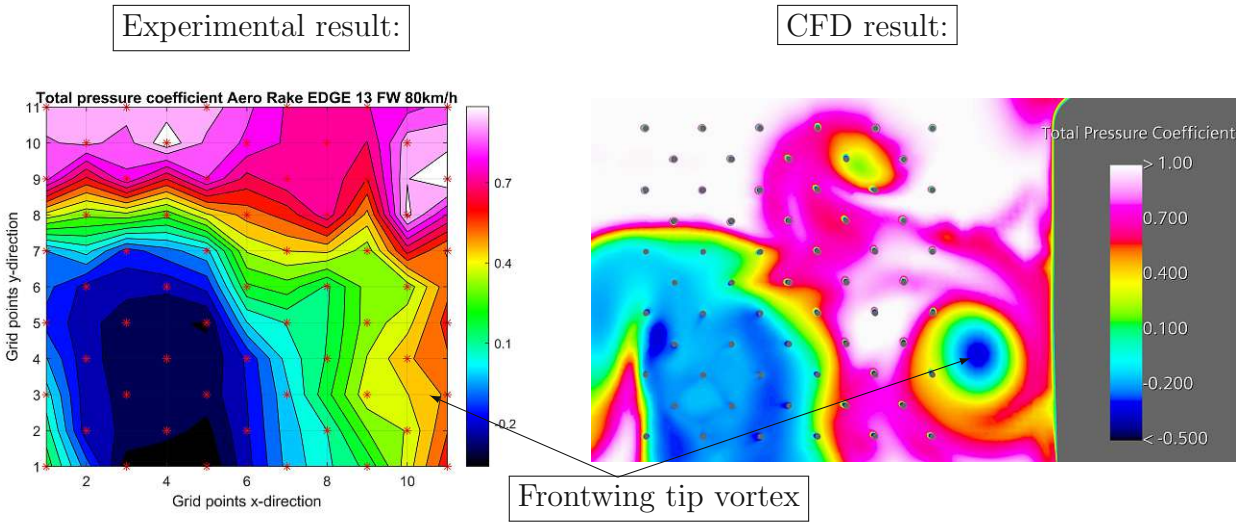

Figure 3.18 – Comparison of experimental rake results and CFD results with the EDGE 13 frontwing

3.2 Pressure Taps

Another way to validate the CFD calculated flow is to directly measure the pressure at aerodynamically important surfaces. This form of validation can be permanently mounted inside the vehicle, as it is common practice in Formula 1. For example, at the 2017 Abu Dhabi Grand Prix, McLaren Honda Engineers noticed a stalling diffuser during the race which was caused by duct tape wrapped around a diffusor vane [12]. For the measurements little holes are drilled (< 1 mm) at the desired position and then a tube is inserted which connects to a pressure scanner. Figure 3.19 shows the circled and numbered pressure taps of the Ferrari SF70H frontwing.

As the undertray generates 40 % of the downforce it is the most import aerodynamic component of the EDGE 14. Therefore it is important to know if the peak low pressure results from CFD are correct. 8 pressure taps have been installed in the right undertray mainfoil as you can see in Figure 3.20. The same pressure sensor as with the aero rake is used and positioned very close to the measurement points to prevent inaccuracies. The positions were chosen at points where low pressure peaks and surface pressure changes. These positions were specified in CAD and then drilled exactly at these places on the component itself. Similar to the rake validation procedure the real life experiment has to be recreated in CFD with the right vehicle attitude and speed. These values are again gathered from the live telemetry. For the pressure measurement in CFD, the

Figure 3.19 – Pressure taps on the SF70H frontwing, source: [9]

coordinates of the taps are needed when the vehicle operates at its constant velocity ride height. Therefore, a CAD model has been designed where the front and rear ride height can be input and the adjusted pressure tap coordinates are obtained as you can see in Figure 3.21.

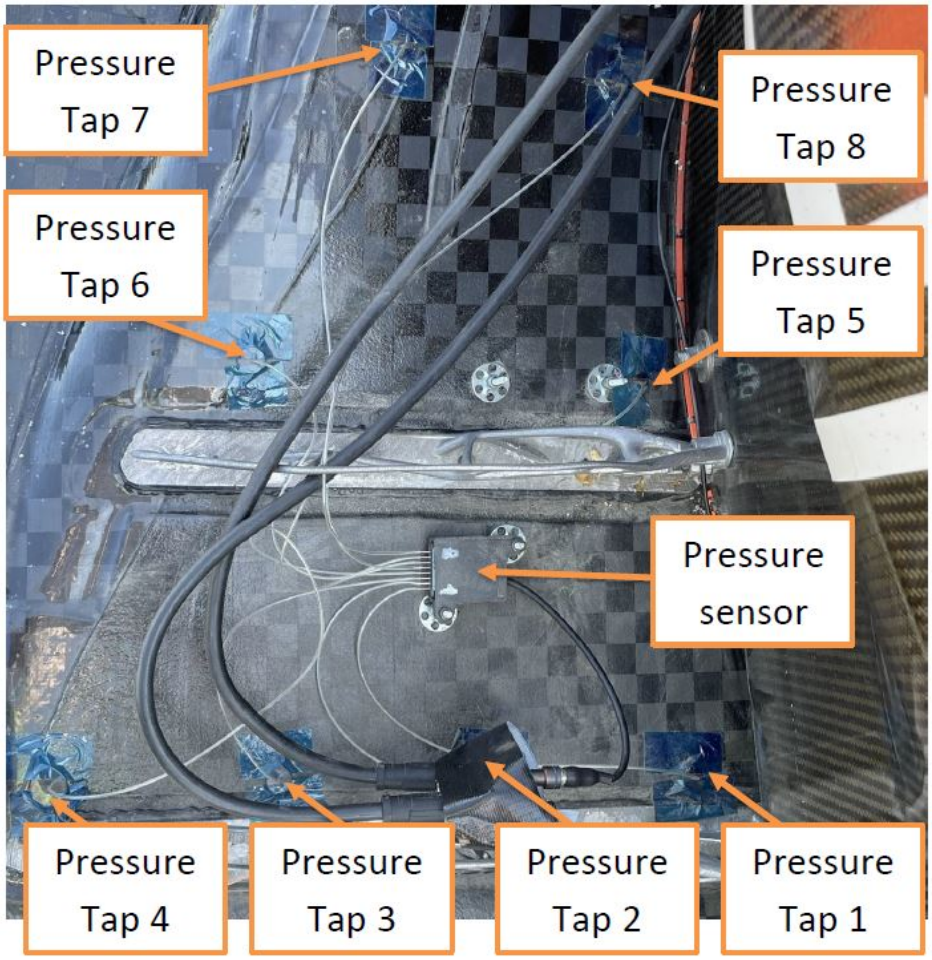

Figure 3.20 – Pressure taps and pressure scanner mounted on undertray mainfoil

With the gathered vehicle attitude, speed and tested geometry, the CFD simulation can be executed. The pressure tap coordinates are displayed and the static surface pressure of the undertray mainfoil can be seen in Figure 3.22. The pressure values are obtained by means of reports or the graphical solution as shown in Figure 3.22.

3.2.1 Pressure taps experimental data acquisition

In order to compare the obtained surface pressures to the straightline CFD simulation, a series of runs with different velocities is conducted. After each straightline run it is being checked if the driver was able to hold the desired constant velocity and the resulting front (FRH) and rear ride height (RRH). Like in previous chapters, this piece of information is gathered using the live telemetry. The resulting vehicles attitudes can be viewed in Table 3.1. It only represents runs where the averaged velocity was

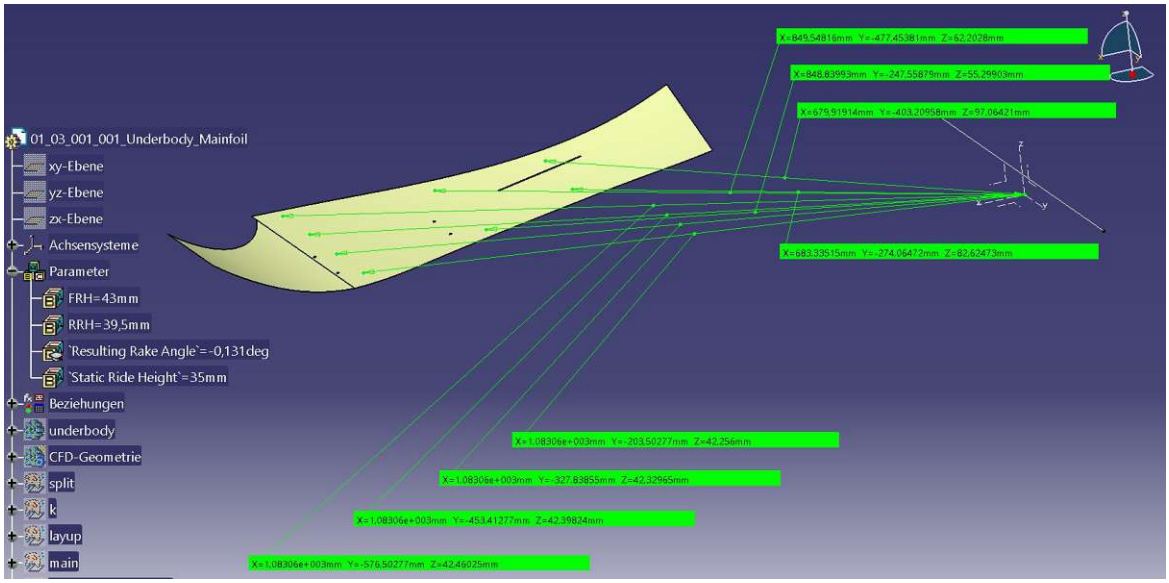

Figure 3.21 – Pressure tap coordinates adjusted by ride heights

within 5% of the desired velocity. It is very interesting to see the spring compression with rising velocity due to rising downforce. With the information of spring travel and velocity the resulting downforce could be calculated using the spring constant. This would be another useful form of validation in order to make sure that the magnitude of downforce is similar to the obtained simulation result. A more practical approach would be to put weight on the aerodynamic components and the standing vehicle until the desired spring travel is achieved. The spring travel at a certain velocity is known and if the load at this certain spring travel equals the aerodynamic load at this velocity, the simulation is accurate.

The obtained surface pressures during straightline are logged in the live telemetry and are averaged to compensate for measuring errors. Furthermore, the surface pressures at 0 km/h are also averaged in order to have the correct reference pressure for each run. Afterwards the static pressure can be calculated using this expression:

$$p_{static} = p_{measured} - p_{reference} \tag{3.3}$$

The gathered static pressures can be seen in Table 3.2. Unfortunately, pressure tap 2 had some faulty measurements, which are specifically visible in run 4, 7 and 10, where partly very low static pressure or positive pressure was detected. A first good sign to indicate the correctness of the data is that all signs are negative and therefore the

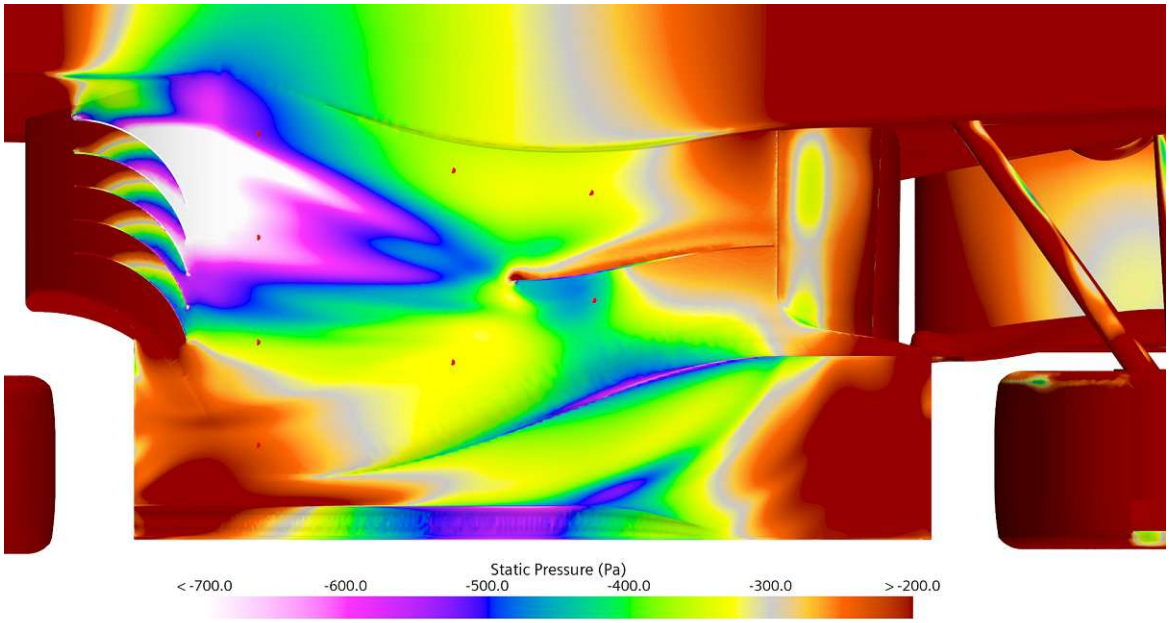

Figure 3.22 – Static pressure and pressure taps (red dots) displayed on undertray mainfoil

local pressure is lower than the ambient pressure. The other thing which speaks for the quality of the data is the steady decrease in static pressure with rising velocity.

3.2.2 Pressure taps CFD data acquisition

To compare the obtained experimental static pressures with simulation results, the real life experiment has to be recreated in CFD. A simulation for each velocity has to be set up, each with the correct vehicle attitudes as displayed in Table 3.1. With the parametric CAD model (Figure 3.21) the exact position of the pressure taps at the simulated ride heights can be displayed in the solution. Furthermore, the static pressure values can be obtained using reports or the graphical solution as shown in Figure 3.22. In order to check the resulting static pressure, for example for the simulation with 80 km/h and pressure tap 1, the limits of the colorbar can be adjusted around the obtained value. Then the point of pressure tap 1 should be within the colors, ergo inside the limits, and the value is correct. For pressure tap 1 with 80 km/h the resulting static pressure is -760 Pa and the graphical check can be seen in Figure 3.23. It is also clearly visible that the pressure tap below, which is pressure tap 2, is exceeding the lower limit, so the static pressure is lower than at pressure tap 1. For all other 6 pressure taps the opposite is true.

Run	Desired velocity [km/h]	Averaged velocity [km/h]	FRH [mm]	RRH [mm]
1	50	49.86	39.2	41.75
2	50	50.58	39.2	41.75
3	50	48.42	39.2	41.75
4	60	59.94	37.8	40.4
5	60	62.46	37.8	40.4
6	60	62.46	37.8	40.4
7	70	69.66	36	39.5
8	70	69.3	36	39.5
9	70	69.84	36	39.5
10	80	84.06	33	37.2
11	80	84.06	33	37.2
12	80	81.18	33	37.2
13	80	80.2	33	37.2
14	90	90	33	36.6
15	90	91.08	33	36.6
16	100	103.14	29.75	34.2
17	110	110.52	27.75	31.65

Table 3.1 – Vehicle attitudes during pressure tap validation runs

The static pressures at different velocities obtained by CFD calculations can be seen in Table 3.3.

When comparing these results with the measured static pressures in Table 3.2 it is clearly visible that there is a problem with pressure tap 2.

3.2.3 Comparison of pressure tap results

In order to compare the experimental and CFD results, the relative error is calculated:

$$error = \frac{p_{CFD} - p_{experiment}}{p_{CFD}} \tag{3.4}$$

The resulting relative error for every measurement at every run can be seen in Table 3.4.

It is now obvious that pressure tap 2 had a problem. It is very likely that the opening of the tube inside the undertray mainfoil was partly closed and therefore wrong results occurred. A less likely option is that channel 2 of the pressure scanner is damaged. This is very unlikely because pressure tap 2 outputs correct results at the rake validation, which was done minutes before the pressure tap validation and no changes were con-

Run	Tap 1	Tap 2	Tap 3	Tap 4	Tap 5	Tap 6	Tap 7	Tap 8
1	-157	-451	-142	-78	-145	-125	-124	-128
2	-211	-360	-183	-110	-185	-179	-141	-162
3	-217	-379	-183	-110	-183	-185	-148	-163
4	-307	47	-253	-149	-262	-242	-228	-224
5	-326	-413	-261	-157	-273	-254	-233	-229
6	-317	-546	-249	-148	-260	-236	-225	-225
7	-433	106	-329	-215	-359	-342	-314	-289
8	-446	-175	-327	-210	-362	-339	-307	-292
9	-444	-140	-338	-219	-375	-345	-307	-289
10	-752	-4	-530	-379	-560	-488	-445	-460
11	-693	-497	-506	-319	-560	-467	440	-427
12	-689	-529	-518	-328	-523	-502	-445	-448
13	-656	-819	-485	-319	-469	-476	-425	-405
14	-931	-536	-653	-414	-649	-616	-550	-482
15	-901	-643	-640	-420	-664	-583	-544	-502
16	-1326	-431	-848	-519	-838	-756	-619	-601
17	-1484	-685	-1040	-662	-950	-1371	-704	-682

Table 3.2 – Measured static pressure in Pa at undertray mainfoil (rounded to 0 decimal places, further calculations are conducted with exact values)

Velocity [km/h]	Tap 1	Tap 2	Tap 3	Tap 4	Tap 5	Tap 6	Tap 7	Tap 8
50	-244	-308	-181	-122	-179	-178	-168	-163
60	-366	-452	-263	-178	-257	-254	-263	-233
70	-523	-662	-367	-236	-355	-326	-444	-334
80	-760	-914	-540	-341	-492	-480	-506	-435
90	-924	-1104	-648	-403	-586	-553	-725	-558
100	-1256	-1490	-875	-545	-780	-761	-691	-655
110	-1650	-1890	-1060	-670	-950	-920	-800	-780

Table 3.3 – CFD calculated static pressure in Pa at undertray mainfoil

ducted at the software or the scanner itself. However, for all the following calculations pressure tap 2 is not taken into account.

When averaging the obtained errors per run (without pressure tap 2), no correlation between rising velocity and error magnitude can be seen in Table 3.5. This means the obtained difference between CFD simulation and reality is independent of the velocity magnitude. In order to prevent the sign of error from misleading the statistics, the averaged magnitude error is also calculated, where the absolute value of each error is averaged. The problem with the averaged error is that one measurement with -50.0 % and another one with 50.0 % would result in an average error of 0.0 % and in an averaged magnitude error of 50.0 %. For this calculation pressure tap 6 of run 17 is also

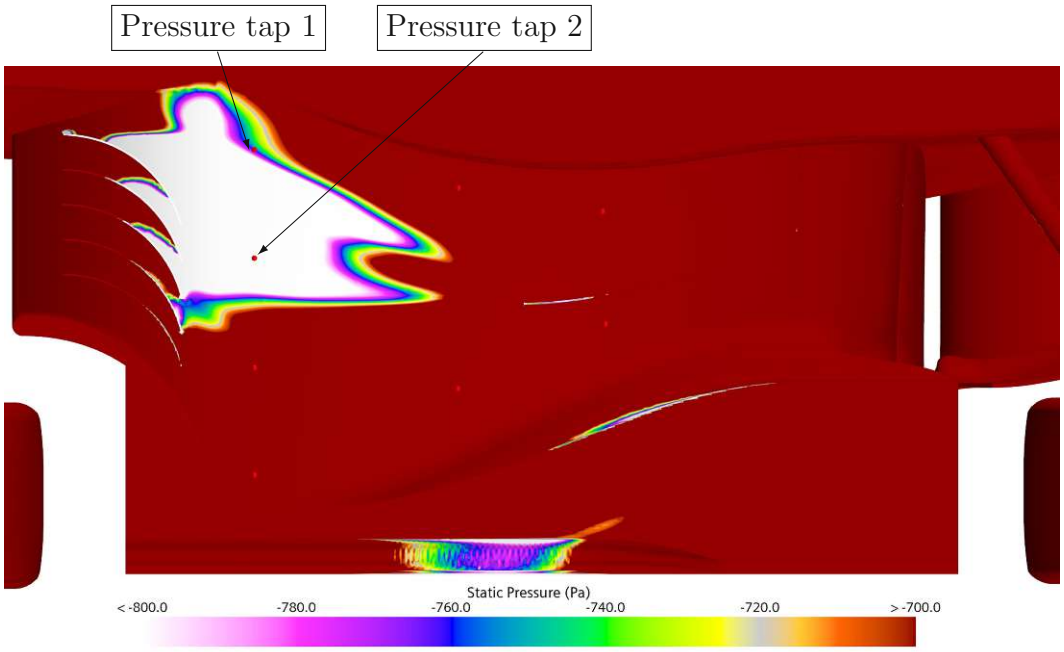

Figure 3.23 – Check if the reported static pressure is at the right coordinates (pressure tap 1 is in the top left corner)

not taken into account, as there was clearly a problem with the measurement because the error is 49.0 %.

The averaged error of each run is positive or slightly negative. This leads to the conclusion that the CFD calculated surface pressure is lower than in reality. Unfortunately, that means, that the undertray produces less downforce than calculated in CFD. The accuracy of the measurements is astonishing when viewing run 7, 8 and 9, where the driver did a great job of managing a constant velocity close to the desired one. The magnitude of the relative difference between experimental results and CFD result stayed within 0.2 %. With this obtained knowledge run 10 and 11 should also provide equal results as they are measured with the same averaged velocity. However, there is clearly a difference in magnitude of 0.9 %. When having a closer look at the velocities of the runs, it can be seen that they are equal concerning averaged velocity but are looking completely different, as you can see in Figure 3.24. This could be one reason why the measurements are not equal even though the average velocity is the same.

Another reason why CFD and experimental results are showing differences is that the vehicle model can have geometrical flaws compared to the CAD model. If these flaws are in aerodynamically important areas, then the flow can be influenced a lot, especially downstream.

Run	Tap 1	Tap 2	Tap 3	Tap 4	Tap 5	Tap 6	Tap 7	Tap 8
1	35.7 %	-46.6 %	21.5 %	36.1 %	19.0 %	29.8 %	26.2 %	21.5 %
2	13.6 %	-16.9 %	-1.1 %	9.8 %	-3.4 %	-0.6 %	16.1 %	0.6 %
3	11.3 %	-23.1 %	-1.1 %	9.8 %	-2.2 %	-3.9 %	11.9 %	0.0 %
4	16.2 %	110.4 %	3.8 %	16.3 %	-1.9 %	4.7 %	13.3 %	4.0 %
5	11.1 %	8.6 %	0.7 %	11.8 %	-6.2 %	0.1 %	11.4 %	1.7 %
6	13.4 %	-20.8 %	5.2 %	16.9 %	-1.3 %	6.9 %	14.4 %	3.6 %
7	17.2 %	116.0 %	10.4 %	9.0 %	-1.2 %	-4.8 %	29.2 %	13.6 %
8	14.7 %	73.6 %	10.9 %	11.1 %	-2.1 %	-4.1 %	31.0 %	12.5 %
9	15.2 %	78.8 %	7.8 %	7.1 %	-5.5 %	-5.6 %	30.8 %	14.5 %
10	1.1 %	99.6 %	1.9 %	-11.0 %	-13.8 %	-1.6 %	12.0 %	-5.6 %
11	8.8 %	45.6 %	6.4 %	6.6 %	-13.7 %	2.8 %	13.0 %	1.9 %
12	9.4 %	42.1 %	4.1 %	3.9 %	-6.2 %	-4.6 %	12.0 %	-2.9 %
13	13.7 %	10.4 %	10.2 %	6.5 %	4.6 %	0.9 %	16.0 %	6.8 %
14	-0.8 %	51.4 %	-0.8 %	-2.7 %	-10.8 %	11.3 %	24.1 %	13.6 %
15	2.5 %	41.7 %	1.2 %	-4.1 %	-13.3 %	-5.4 %	25.0 %	10.1 %
16	-4.8 %	71.1 %	3.1 %	4.7 %	-7.5 %	0.7 %	10.4 %	8.3 %
17	10.1 %	63.7 %	1.9 %	1.2 %	0.0 %	-49.0 %	12.0 %	12.6 %

Table 3.4 – Comparison between experimental and CFD pressure tap results

In order to know if a specific pressure tap is predicted wrongly in CFD, all relative errors of each pressure tap are averaged and also again averaged in magnitude. The results are displayed in Table 3.6. When looking at Table 3.6 it is visible why pressure tap 2 was not taken into account at previous evaluations. Furthermore the static pressure is predicted very well, except at pressure tap 7. The obtained static pressure at tap 7 is significantly higher than the CFD result at each run. Therefore a flow phenomenon is predicted incorrectly, or the measurement channel of tap 7 has an offset error.
When averaging all magnitude errors of all runs and all taps, except pressure tap 2 and tap 6 run 17, then an averaged magnitude error of 9.3 % results.

Run	Desired velocity [km/h]	Averaged velocity [km/h]	Averaged error	Averaged magnitude error
1	50	49.86	27.1 %	27.1 %
2	50	50.58	5.0 %	6.5 %
3	50	48.42	3.7 %	5.8 %
4	60	59.94	8.0 %	8.6 %
5	60	62.46	4.3 %	6.1 %
6	60	62.46	8.4 %	8.8 %
7	70	69.66	10.5 %	12.2 %
8	70	69.3	10.6 %	12.3 %
9	70	69.84	9.2 %	12.4 %
10	80	84.06	-2.4 %	6.7 %
11	80	84.06	3.7 %	7.6 %
12	80	81.18	2.2 %	6.2 %
13	80	80.2	8.4 %	8.4 %
14	90	90	1.6 %	9.1 %
15	90	91.08	2.3 %	8.8 %
16	100	103.14	2.1 %	5.6 %
17	110	110.52	-1.6 %	6.3 %

Table 3.5 – Averaged error of pressure tap validation runs

	Tap 1	Tap 2	Tap 3	Tap 4	Tap 5	Tap 6	Tap 7	Tap 8
Averaged error	11.1 %	41.5 %	5.1 %	7.8 %	-3.9 %	5.5 %	18.2 %	6.9 %
Averaged magnitude error	11.7 %	54.1 %	5.4 %	9.9 %	6.6 %	0.2 %	18.2 %	7.9 %

Table 3.6 – Averaged error of the pressure taps (pressure tap 6 run 17 not taken into account)

Figure 3.24 – Velocities of run 10 and run 11

4

Conclusion

In order to analyse the flow around the Formula Student vehicle EDGE 14, a straightline halfcar CFD Simulation has been set up. It has been shown that the usage of the low wall y+ approach and therefore properly resolving the viscous sublayer at aerodynamic components is essential to make sure that the boundary layer does not separate. Furthermore, when looking at the results of the CFD simulation with the usual base size of 33 mm, a discretization error has to be taken into account. This error can be reduced by making sure that the grid is fine enough.

The experimental results have shown that the quality of the CFD simulation is very good. Flow features are in reality exactly where they were predicted to be. Specifically the bullhorn vortex in Figure 3.14 and the transition from high energetic flow to low energetic tyre wake in Figure 3.15 were really accurate predictions. The rake validation has also shown that the transition above the tyre wake to the freestream flow is exactly where CFD predicts it to be. It has also been proven that different geometries, as the EDGE 13 frontwing and EDGE 14 frontwing, produce different flow features, which are resolved correctly by the k-ω turbulence model. The usage of the live telemetry and the ride height sensors is essential to reconstruct the experimental result in CFD. Further studies could be carried out using different turbulence models, such as the k-ϵ or Spalart Allmaras models. It would also be interesting to step away from Reynolds averaged Navier-Stokes equations and compare the rake results to Large Eddy simulation or Detached Eddy simulations. Another approach worth being tried would be putting the aero rake behind the rear tyre as there are more turbulences generated in front of the rear tyre. The prediction of the flow is going to be much more difficult than behind the front tyre. As you can see the possibilities for using an aero rake for validation purposes seem to be endless.

The last form of validation was the usage of pressure taps. These are mounted on the low pressure side of the undertray mainfoil. As indicated in Figure 3.20, tubes connected to the pressure scanner are guided through the mainfoil itself to measure the local static pressure on the suction side. 17 runs have been carried out at different velocities and therefore at different ride heights. The vehicle attitudes were used to set up CFD simulations representing this exact state and the resulting comparison of obtained values can be viewed in Table 3.5. The knowledge was gathered that the CFD calculations result in less static pressure than in reality. Therefore not as much downforce is generated at the EDGE 14's undertray mainfoil. For future pressure tap validations, a pitot tube to measure the freestream pressure would be ideal in order to be able to compute the pressure coefficient. To gather valuable information about the flow, the frontwing mainfoil or rearwing mainfoil could also be equipped with these taps.

Bibliography

[1] Wimshurst A. Fluid mechanics 101 calculators tools, .

[2] Wimshurst A. Fluid mechanics 101 cfd for professionals, .

[3] R. Anderl and P. Binde. *Simulations with NX/Simcenter 3D: kinematics, FEM, CFD, EM and data mangement.* München : Carl Hanser Verlag GmbH Co. KG © 2018, 2018.

[4] Blocken B. *LES over RANS in building simulation for outdoor and indoor applications: A foregone conclusion?* Springer, 2018.

[5] Launder B. and Spalding D. *The numerical computation of turbulent flows.* AIAA Journal, 1974.

[6] Menter F. *Two-equation eddy-viscosity turbulence models for engineering applications.* AIAA Journal, 1994.

[7] J. H. Ferzinger, M. Peric, and R. Street. *Computational Methods for Fluid Dynamics.* Cham: Springer International Publishing : Imprint: Springer, 2020.

[8] Kiel G. *Total-Head Meter with small sensitivity so yaw.* Technical Memorandums National Advisory Committee for Aeronautics, 1935.

[9] https://au.motorsport.com/f1/news/brazilian-gp-tech-2018-mercedes-ferrari-red-bull 978618/1378569/. Tech analysis: The 2018 f1 season starts here. Accessed: (14.9.2023).

[10] https://docs.sw.siemens.com/de DE/doc/226870983/PL20210401101005144.starccmp$_u serguide_h t$ $ccm + -userguide. Accessed$: (8.9.2023).

[11] https://www.evolutionmeasurement.com/wp-content/uploads/2019/07/EvoScann Datasheet-P8A.pdf. P8-a absolute mode pressure scanners. Accessed: (11.9.2023).

[12] https://www.f1technical.net/features/21652. Evolution of aerodynamic testing in f1 - measurements. Accessed: (14.9.2023).

[13] https://www.formula1.com/en/latest/article.smedley-what-are-aero rakes.1F74d3YVUBzRRiZz9D3nZ4.html. Testing explained: Rob smedley on aero rakes. Accessed: (9.9.2023).

[14] https://www.formulastudent.de/fsg/rules. Formula student rules 2023. Accessed: 7.9.2023.

[15] Celik I., Ghia U., Roache P., Freitas C., Coleman H., and Raad P. *Procedure for Estimation and Reporting of Uncertainty Due to Discretization in CFD Applications.* Journals of Fluids Engineering Vol. 130 / 078001-3, 2008.

[16] Gharbi N., Absi R., Benzaoui A., and Amara E. *Effect of near-wall treatments on airflow simulations.* Proceedings of 2009 International Conference on Computational Methods for Energy Engineering and Environment: ICCM3E, 2009.

[17] Kovacs P. *Entwicklung einer Aero Rake für die Analyse der Aerodynamik eines Formula Student Rennwagens.* 2020.

[18] Jayanti S. *Computational Fluid Dynamics for Engineers and Scientists.* Springer Science+Business Media, 2018.

[19] McBeath S. *Competition Car Aerodynamics.* Veloce Publishing Limited, 2015.

[20] H. Schlichting and K. Gersten. *Boundary-Layer Theory.* Berlin, Heidelberg : Springer Berlin Heidelberg : Imprint: Springer, 2017.

[21] A. Sharma. *Introduction to Computational Fluid Dynamics.* Springer Nature Switzerland AG, 2022.

[22] Briet T. *Aerodynamic Definitions 1 Motorsport Engineering Aerodynamic Knowledge.* Independently published, 2023.

[23] Briet T. *Wind Tunnels and Theoric CFD: Design and Useful Motorsport Engineering Aerodynamic Knowledge 9.* Independently published, 2023.

[24] Briet T. *Aerodynamic Principles and Consequences 2 Motorsport Engineering Aerodynamic Knowledge*. Independently published, 2023.

[25] J. Tu, G. Yeoh, and C. Liu. *Computational Fluid Dynamics- A practical Approach (3rd Edition)*. Saint Louis:Elsevier, 2018.

[26] Cengel Y. and Cimbala J. *Fluid Mechanics: Fundamentals and Applications*. McGraw-Hill, 2006.

List of Figures

List of Tables